THEMIS ESA First Science Results and Performance Issues

J. P. McFadden, C. W. Carlson, D. Larson, J. Bonnell, F. Mozer, V. Angelopoulos, K.-H. Glassmeier, U. Auster

University of California
Space Sciences Laboratory
7 Gauss Way
Berkeley, CA 94720

mcfadden@ssl.berkeley.edu
510-642-9918 office
510-643-8302 fax

THEMIS ESA First Science Results and Performance Issues

Abstract

Early observations by the THEMIS ESA plasma instrument have revealed new details of the dayside magnetosphere. As an introduction to THEMIS plasma data, this paper present observations of plasmaspheric plumes, ion conic outflows, field line resonances, structure at the low latitude boundary layer, flux transfer events at the magnetopause, and wave and particle interactions at the bow shock. These observations demonstrate the capabilities of the plasma sensors and the synergy of its measurements with the other THEMIS experiments. In addition, the paper includes discussions of various performance issues with the ESA instrument such as sources of sensor background, measurement limitations, and data formatting problems. These initial results demonstrate successful achievement of all measurement objectives for the plasma instrument.

Keywords
THEMIS, Magnetosphere, Magnetopause, Bow Shock, Instrument Performance

Classification System
94.80.+g
06.20.fb
94.30.C-
94.05.-a
07.87.+v

1.0 Introduction

The THEMIS mission provides the first multi-satellite measurements of the dayside magnetosphere, magnetopause and bow shock with a string of pearls orbit near the ecliptic plane (Angelopoulos et al., 2008). Each THEMIS spacecraft includes a fluxgate magnetometer (Auster et al., 2008), a search coil magnetometer (Roux et al., 2008), a 3-axis electric field instrument (Bonnell et al., 2008), solid state telescopes (SST) for energetic (>30 keV) ions and electrons (Larson et al., 2008), and electrostatic analyzers (ESAs) for electron and ion plasma (<30 keV) measurements (McFadden et al., 2008a). These instruments not only provide the information needed to perform substorm timing analysis during the prime mission, but also provide a core set of measurements needed to resolve most magnetospheric dynamics. In this paper we will highlight the measurement capabilities of the ESA plasma sensors by presenting "first results" from several regions in and around the magnetosphere. Although plasma measurements will be the focus of these first results, observations from the other sensors are included to illustrate the synergy of these measurements and to demonstrate the ability of THEMIS satellites to resolve the basic plasma features of these regions. Throughout the paper we refer to the individual satellites by their abbreviated call letters – THA, THB, THC, THD and THE.

The THEMIS plasma instruments measure the 3-D plasma distribution function with ~3 s resolution. Although the highest-time, highest-phase-space resolution measurements are only available during bursts which are generally limited to ~15 minutes per orbit, coarser 3-D distributions at spin resolution are available for ~12 hours each orbit. These data have adequate angular resolution to allow accurate ground computation of moments and identification of beams. Even during periods where data collection is limited, the ESA data products include on-board calculated moments and omni-directional energy spectra at spin resolution. These on-board moments include corrections for spacecraft charging providing accurate electron moment computations that eliminate photoelectrons. Spin-resolution energy spectra provide the additional information needed to interpret variations in the on-board moments and to correctly identify the dynamics associated with boundaries or changes in the multi-component plasma.

As demonstrated in the accompanying paper (McFadden et al., 2008a), the close proximity of the five THEMIS spacecraft during the early mission allowed very accurate in-flight calibration of the ESA sensors. The relative sensitivities of the ten sensors are believed to be determined to better than 5%, and the absolute sensitivity corrected to ~10% through cross calibration with Wind-SWE. The primary uncertainties in this calibration effort resulted from estimation errors of the proton to alpha ratio of the solar wind, from uncertainties in calculating the spacecraft-to-plasma potential from the measured spacecraft-to-langmuir-probe potential, and by relying on the literature to correct for energy dependent efficiencies of the microchannel plate detectors. However, pressure balance checks across the dayside magnetopause (Figure 16, McFadden et al., 2008a), performed independent of the calibration effort, provide additional confidence in our techniques. These accurate calibrations allow the combined electron and ion data to

be used to deduce additional features about the plasma including mass composition and the presence of missed cold plasma.

During the first 7 months of the THEMIS mission, the five spacecraft sampled the dusk, sub-solar and dawn regions of the magnetosphere. Section 2 presents first results from the encounters with these regions illustrating the abilities of the instruments to resolve small scale features and separate space and time. Although the THEMIS ESAs provide a data set of well calibrated observations, there are still several instrumental limitations to the data. During the course of the presentation, we will point out measurement limitations and uncertainties in the observations that can affect the accuracy of computed products such as moments. Some of these performance issues involve missing information, such as composition, while others are associated with the instrument's dynamic range.

THEMIS has an open data policy that strives for an immediate data release to the community. While data quality flags will be inserted into high level processed data, much of the data analysis effort will utilized unprocessed data. Therefore scientists need a reference where performance issues are identified, such as non-geophysical background counts, or where the impact of missing information, such as composition, is discussed. In section 3 we provide a summary of all known performance issues with the ESA sensor including sources of background, non-ideal response of the instrument, limitations due to missing information, and telemetry formatting problems. Understanding and correcting for these performance issues will allow full use of the THEMIS measurement capabilities while avoiding any misinterpretation of the observations.

2.0 Multi-point observations by THEMIS

The multi-point measurements afforded by the five spacecraft provide the most important advantage of the THEMIS data set. THEMIS observes both the spatial and temporal variations in the structure of the magnetosphere, allowing detailed studies of time varying phenomena. This capability was most clear during the early mission when the spacecraft were organized in a string of pearls orbit that sampled the low latitude dayside magnetosphere. During this period, the spacecraft were ordered THB, THD, THC, THE, and THA, with an apogee of ~14.5 Re and perigee of ~1.13 Re. For magnetopause crossings, the inner three spacecraft were more closely bunched (~1000 km separations) while the lead and trailing satellites were generally separated by much larger (~4000-10000 km) distances from the inner probes. This organization allowed sampling of the magnetopause and bow shock over multiple scales.

Figure 1 shows data from the fluxgate magnetometers and ion ESA sensors on the three inner probes during an outbound magnetopause crossing at ~1330 LT on June 10, 2007. For this crossing, THD was leading THC by ~500 km and THE was trailing THC by ~1350 km. The panels are ordered top-to-bottom as the spacecraft are ordered along the orbit. Ion spectrograms provide clear identifications of changes in the plasma while the magnetometer provides identification of the magnetopause current. Ion velocity, plotted in LMN coordinates, is used to identify features of the boundary layer and

distinguish between sheath flows, reconnection jets, and stagnant sheath plasma. The June 11 crossing was during a period of steady southward interplanetary magnetic field (IMF Bz~-15 nT at the magnetopause from 2130-2204 UT as determined by THB). Although external conditions were relatively constant, the magnetopause shows significant changes in structure on three crossings separated by less than 10 minutes.

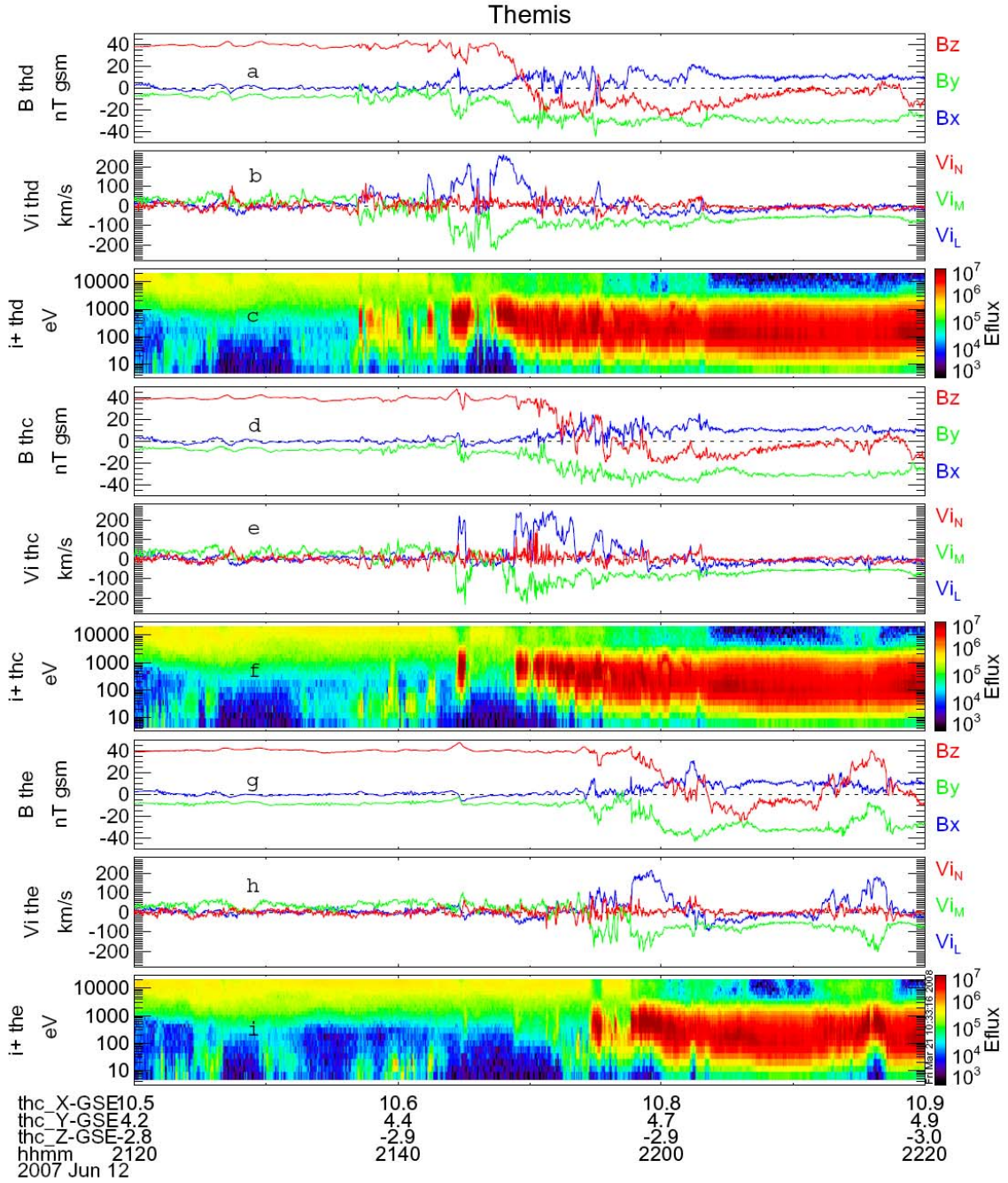

Figure 1: Magnetic field in GSM, ion velocity in LMN, and ion spectrograms for the THD (panels a-c), THC (panels d-f) and THE (panels g-i) spacecraft. The plot shows three closely spaced crossing of the magnetopause during steady southward IMF illustrating the multipoint capabilities of THEMIS spin resolution observations.

The multi-satellite observations by THEMIS provide a time history of the evolution of the magnetopause during low-latitude reconnection. Beginning at the left side of Figure 1, low energy (<100 eV) ions are observed prior to 2137 UT in panel c (<2144 UT in panel f, <2155 UT in panel i). These are cold ions, generally repelled by spacecraft charging, which are revealed by magnetopause motion. Section 2.1 provides a closer look at this cold plasma component and McFadden et al. (2008b) provides a detailed look at cold plasma structure at the magnetopause. In addition to magnetopause motion inferred from cold plasma, multiple undulations of the magnetopause are clearly observed in the THD crossing (panels a-c) between 2137 and 2148 UT. Some of this motion is caused by the passage of flux transfer events (FTE), such as the FTE seen by all three spacecraft at 2145 UT. In section 2.5 we take a closer look at FTEs to illustrate the plasma structure that can be resolved by THEMIS ESAs.

The additional magnetopause crossings by THC (panels d-f) and THE (panels g-i) show a similar overall structure, but differ in details from the THD crossing. In particular, variations in reconnection flow-jet velocities are revealed in panels b, e, and h. Lastly, we note the decrease in dynamic pressure after 2205 UT results in an outward motion of the magnetopause causing THE to re-enter the boundary layer. Even though the sheath Bz has dropped to zero, reconnection flows are still evident at THE (2112-2117 UT). The degree of outward motion can also be partially quantified (~1100 km) since THC sees some hints of magnetospheric ions in boundary layer. In summary, Figure 1 demonstrates the capabilities of THEMIS to resolve structure and dynamics through multipoint measurements with 3 s resolution. Current plans are to have even closer separations for the inner three probes during the extended mission to allow investigations of coherence scales at the magnetopause.

Figure 2 shows an outbound magnetopause crossing on June 10, 2007 during a period of steady northward IMF. For this crossing, THD was leading THC by ~1200 km and THE was trailing THC by ~1800 km. The vertical bars show the outer edge of the boundary layer as identified from the electron distribution (not shown). Heated magnetosheath electrons are a signature of field lines that have reconnected in at least one hemisphere (Fuselier et al., 1995). As in the case of southward IMF, the boundary layer ions showed variations in structure even though the time between each crossing was less than 15 minutes. In particular the thickness of that portion of the boundary layer with fast flows (~100 km/s) in the M-direction seems to be increasing with time.

For this event, it the majority of the fast-flow flux tubes inside the boundary layer had uni-direction electron heating (not shown) indicating only one end of the field line had reconnected in the lobes. These observations, located ~4 Re from the sub-solar point, differ with other THEMIS observations near the sub-solar region (McFadden et al., 2008c) where the majority of flux in the boundary layer have bi-directional heated electrons during northward IMF indicating dual-lobe reconnection. A larger study of the Low Latitude Boundary Layer (LLBL) is needed to quantify the importance of dual-lobe and single-lobe reconnection. Section 2.4 provides a more detailed demonstration of THEMIS's ability to resolve structure in the LLBL, including electron heating.

Additional insight into LLBL formation and evolution using THEMIS data can also be found in Oieroset et al. (2008).

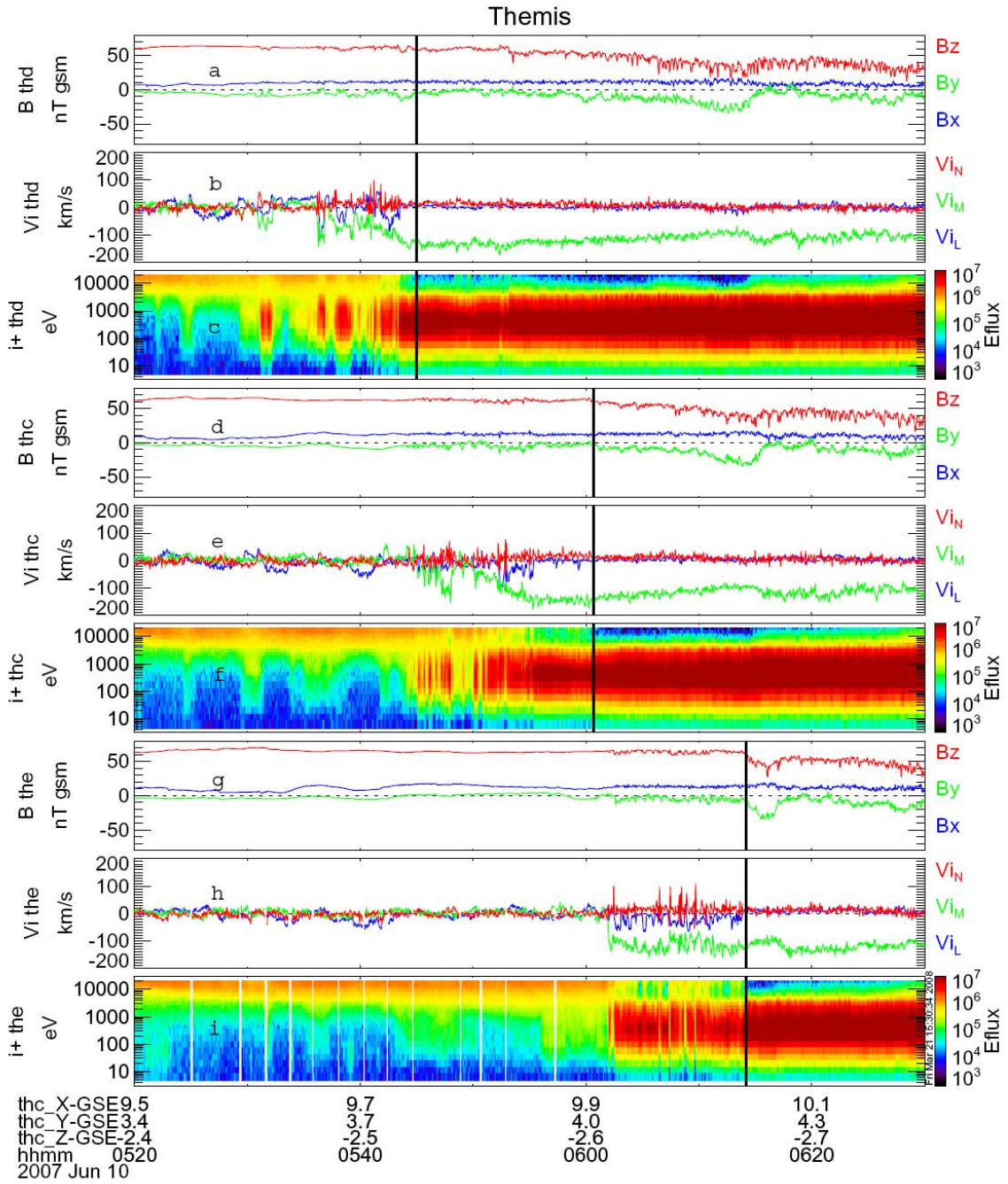

Figure 2: Magnetic field in GSM, ion velocity in LMN, and ion spectrograms for the THD (panels a-c), THC (panels d-f) and THE (panels g-i) spacecraft. The plot shows three closely spaced crossing of the magnetopause during steady northward IMF.

2.1 Plasmaspheric Plumes and Cold Plasma

The plasmasphere, a primary reservoir of magnetospheric plasma, is routinely monitored at 6.6Re by the LANL satellites (Su et al., 2001); however, its extension beyond geosynchronous altitude has not been systematically studied. Magnetospheric convection erodes the outer portions of the plasmasphere creating plasmaspheric plumes that stretch out to the magnetopause. During magnetic storms this loss of plasmaspheric plasma can be quite large as demonstrated vividly by pictures from the IMAGE satellite (Goldstein et al., 2004). In situ measurements of cold ions near the magnetopause have occasionally recorded these losses (Sauvaud et al., 2001), but there has been no comprehensive analysis of plasmaspheric plume morphology and dynamics, of its participation in dayside reconnection, or of the role these losses play in global mass circulation. THEMIS, with its string or pearls configuration, provides the opportunity to observe the evolution of plasmaspheric plumes under a variety of solar wind conditions. The near equatorial orbits provide a large volume of data on these outflows, demonstrating the increasingly important role that cold plasma plays in magnetospheric dynamics.

Figure 3 illustrates a high density cold plasma plume observed by the THC spacecraft that extended from the plasmasphere to within ~0.5 Re of the magnetopause. The upper three panels show the magnetic field, and electron and ion spectrograms as the spacecraft traveled outbound from near geosynchronous to the magnetosheath. Panel d shows the measured ion (black) and electron (red) densities, and the density inferred from spacecraft potential (green). Due to measurement limitations discussed below, the inferred density (green) provides the best measure of actual plume density. The cold plasma plume dominates the density, varying between $10/cm^3$ and $50/cm^3$, before abruptly decreasing to less than the hot plasma density ($\sim 0.3/cm^3$) just before 2230 UT.

The lower panels of Figure 3 zoom in on a region where cold ions can be measured. Panels e-h show electron and ion spectrograms, ion velocity, and density. Spacecraft potential is indicated by the black line on the electron spectrogram. The black line on the ion spectrogram is the proton energy at the drift velocity. Density and velocity calculations include corrections for spacecraft potential, and ion moments are calculated assuming only protons. Cold ions are seen in panel f when the plasma flow velocity is high enough (>50 km/s) so that protons can overcome the retarding barrier resulting from spacecraft charging. As seen between 2202 UT and 2204 UT, these ions often appear as a narrow spectral peak whose changing energy indicates acceleration of the bulk plasma. Flows this large are often observed near the magnetopause, where changes in solar wind dynamic pressure cause substantial motion of this boundary and the nearby plasma.

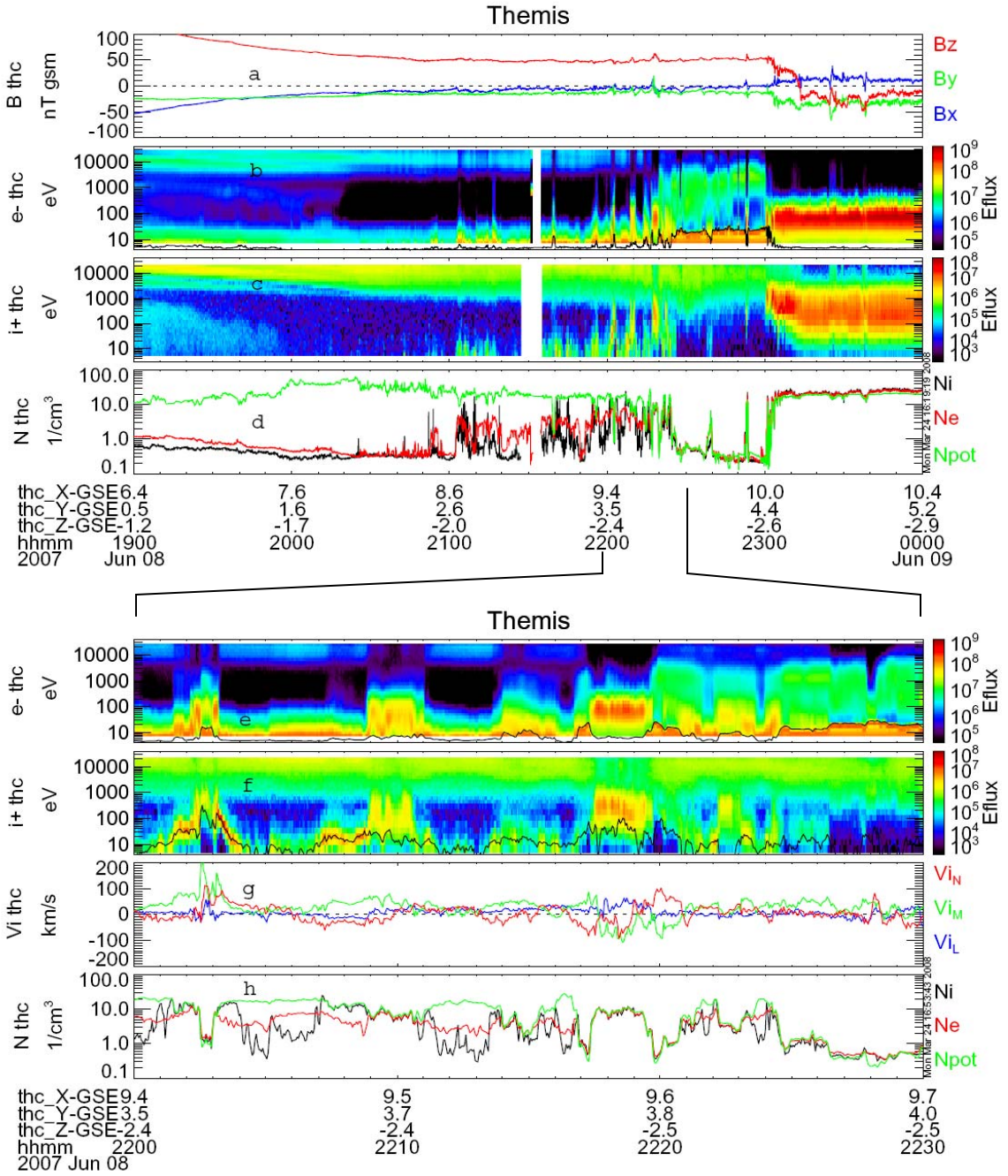

Figure 3: a) Magnetic field, b) electrons c) ions and d) density. The three density curves include the measured ion (black) and electron (red) densities, and the inferred density (green) from spacecraft potential. A high density plume (>10/cm^3) extends from the plasmasphere to within ~0.5 Re of the magnetopause. The lower panels zoom in to the outer edge of the plume illustrating the e) electrons, f) ions, g) ion velocity, and h) density. The black line on panels b and e indicate the spacecraft potential and the black line on panel f indicates the energy of protons at the ion flow velocity minus eΦ_{sc}. Figure adapted from McFadden et al., 2008b.

Although some agreement is observed between the electron (red), ion (black), and inferred (green) densities in panel h, there are many periods where calculated densities differ significantly from the inferred density. These disagreements illustrate two measurement limitations of the THEMIS ESA that result in missed cold plasma and demonstrate the importance of spacecraft potential inferred density. The first limitation is a consequence of spacecraft charging which prevents cold ions from reaching the sensor. Only when the convective flow is large enough so that cold protons can penetrate the spacecraft potential barrier will the ion density be correct. When the black line in panel b, which indicates the energy of protons at the ion flow velocity minus $e\Phi_{sc}$, drops near or below the lowest energy measured, as at 2204-2207 UT, cold ions will be missed by the ion sensor resulting in a measurement error.

The second measurement limitation occurs when the spacecraft potential, black line in panel a, drops below the lowest energy measured by the electron sensor, as at 2203-2209 UT and 2211-2214 UT. During these periods cold electrons, which neutralize the cold ions, are missed by the electron sensor. Missed cold electrons at 2207-2209 UT result in a measured ion density greater than the measured electron density. Of course both densities were actually equal, and the discrepancy results from our measurement limitations. This limitation to the electron measurement can be fixed by sweeping the sensor to lower energy, as is currently planned for the second year.

The multi-satellite THEMIS measurements provide global context for plasmaspheric plume studies. All 5 THEMIS spacecraft observed this plume, measuring high-densities ($>10/cm^3$) and simultaneous magnetopause motions. Similar high-density plumes have been observed on at least 15 orbits, with the highest density plume having $\sim 60/cm^3$ near the magnetopause. In addition, cold plasma with density $>2/cm^3$ (nearly an order of magnitude greater than the hot plasma) was observed at distances >8 Re on all THC orbits in June, 2008, in the post-noon sector. A more in depth look at these cold plasma plumes can be found in McFadden et al. (2008b).

2.2 Ionospheric conic outflows

Ionospheric outflows in the form of ion beams and conics are a significant source of plasma to the plasmasheet (Yau et al., 1985) and the lobes (Moore, 1991). Most of these outflows originate in the low-altitude auroral oval where ions are energized and ejected into most regions of the magnetosphere. These ions provide a significant contribution to mass loading of the magnetosphere, and as such are an important part of the overall magnetospheric plasma circulation. Although contributions of ionospheric outflows have been measured by previous missions (Lennartsson and Shelley, 1986), the THEMIS mission offers the unique ability to capture and quantify these outflows using multipoint measurements. The following discussion provides a quick look at the general features of these outflows at THEMIS altitudes.

Unlike the cold ions (section 2.1) which are primarily observed with velocities perpendicular to the magnetic field during enhanced convection, ionospheric ion outflows generally form a broader energy “cool” component that consists of field aligned ions

which are detected independent of convection. Since ion conics and beams are produced at low altitudes, they both fold up in pitch angle into narrow field-aligned beams as they move to the equatorial regions at THEMIS making it virtually impossible to distinguish between them from their angular signature. Conics and beams may be distinguished by their energy spectra, with conics generally much broader in energy, however time variations in beam energy coupled with dispersion generally broaden ion beams. Since ions that make up ion beams generally started out as conics at lower altitudes, for the following discussion we do not attempt to differentiate between the two and refer to all these outflows as conics. A cursory examination of the dayside data indicates these conics are less common than the cold ions, however we expect this to change as the THEMIS spacecraft move into the magnetotail where they can sample auroral ion outflows.

Figure 4 illustrates a conic outflow at ~1340 LT as THD traveled inward from the magnetopause. Conics appear as a broad, low-energy (5-200 eV) band in the ion spectrogram (panel b). They are observed nearly continuously for more than an hour, decreasing slowly in energy with time. Panel c shows that their appearance does not depend on high flow velocities. A more detailed analysis has shown the bulk of their velocity is field-aligned, and sometimes counter-streaming. Panel a demonstrates that the conics are accompanied by a low energy electron component. The bulk of these cool electrons are relatively isotropic, however the electrons >100 eV consist of field-aligned counter-streaming electrons.

Panel d compares measured electron and ion densities, assuming only protons. The hot ion density is only ~0.3/cm^3, therefore the cooler conics dominate the density. The density mismatch illustrates a general problem interpreting THEMIS data when composition is not known. By assuming only protons when calculating the density, the computed fractional density of any non-proton component will be reduced by a factor of $(m_p/m_i)^{1/2}$, where m_i is the component's mass and m_p is the proton mass. However, the mismatch could also be due to missed cold ions below the lower energy cutoff of the sensor (~15 eV when spacecraft potential is taken into account).

To test for missed ions we plot the proton energy (black line, panel b), less a correction for spacecraft charging, at the calculated flow velocity (panel c). This curve on the spectrogram allows one to determine whether cold protons below the sensor cutoff energy could explain the density mismatch, assuming "protons only" plasma. The fact that the mismatch occurs even when the black curve in panel b is above the sensor cutoff indicates the "protons only" assumption is incorrect and that either He+ or O+ are present. In addition, if the "protons only" assumption is invalid, then the calculated ion velocity will also be incorrect. (Note that this does not invalidate the above test.) The velocity is overestimated by an amount that depends on the fraction of higher mass components. For the example in Figure 3, the ratio of ~3 for the calculated electron and ion densities indicates that the bulk of the conics are probably O+. Unfortunately it may be impossible to quantitatively untangle the fractional composition for this period. Nonetheless we hope this example illustrates the methodologies and complexities involved in analyzing data without composition information.

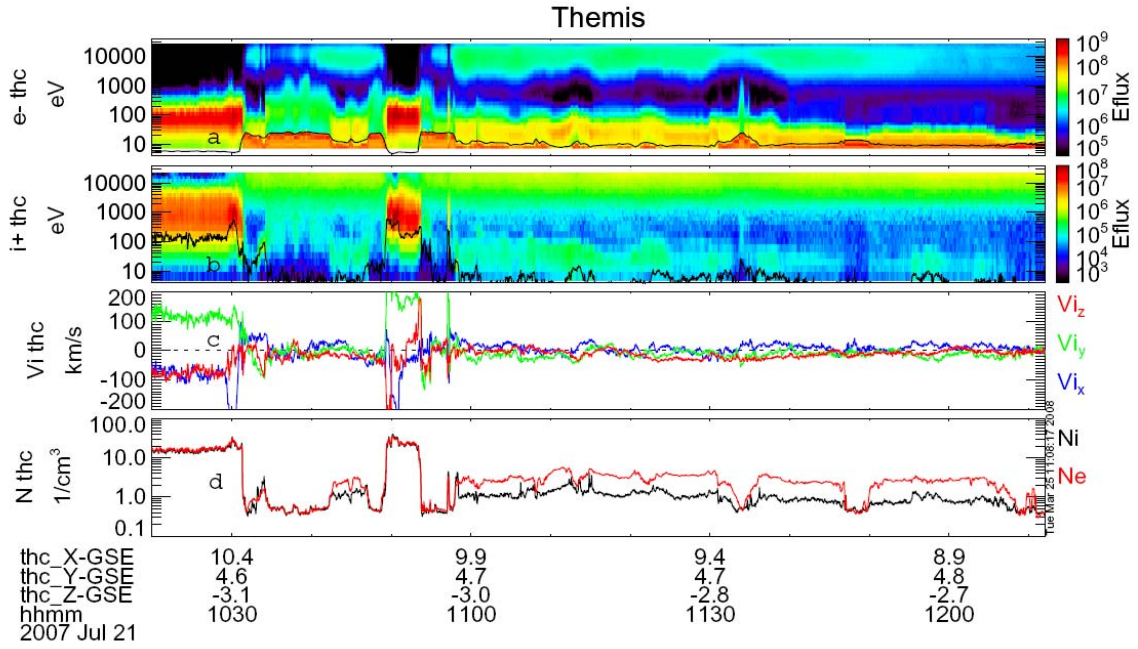

Figure 4: Electron (panel a) and ion (panel b) spectrograms, ion velocity (panel c), and ion (black) and electron (red) densities (panel d) during a conic outflow at ~1340 LT as THD traveled inward from the magnetopause. Conics appear as a broad, low-energy (5-200 eV) band in the ion spectrogram (panel b). The mismatch in ion and electron densities is caused by an error in the ion density calculation resulting from a "protons only" assumption. The conics are most likely O+.

2.3 Pc 5 Field Line Resonances

Azimuthally polarized toroidal Pc 5 pulsations, or field line resonances (FLRs) are commonly observed by THEMIS in the dusk and dawn magnetosphere. These resonances have a magnetic node at the equator where they exhibit large amplitude plasma motions with only small magnetic perturbations. There is no agreed upon source for these waves but it is thought that modulations at the magnetopause, due to Kelvin-Helmholtz instabilities, pressure variations, or changes in reconnection (FTEs), couple energy to these waves. Glassmeier et al. (2008), in a case study of THEMIS multi-satellite measurements, provides an analysis of this coupling that suggests most magnetospheric variations are "quasi-static responses to pressure induced magnetopause motions". These FLRs are often observed to grow in amplitude with one phase relationship between the velocity components, then decay away with a different phase relationship.

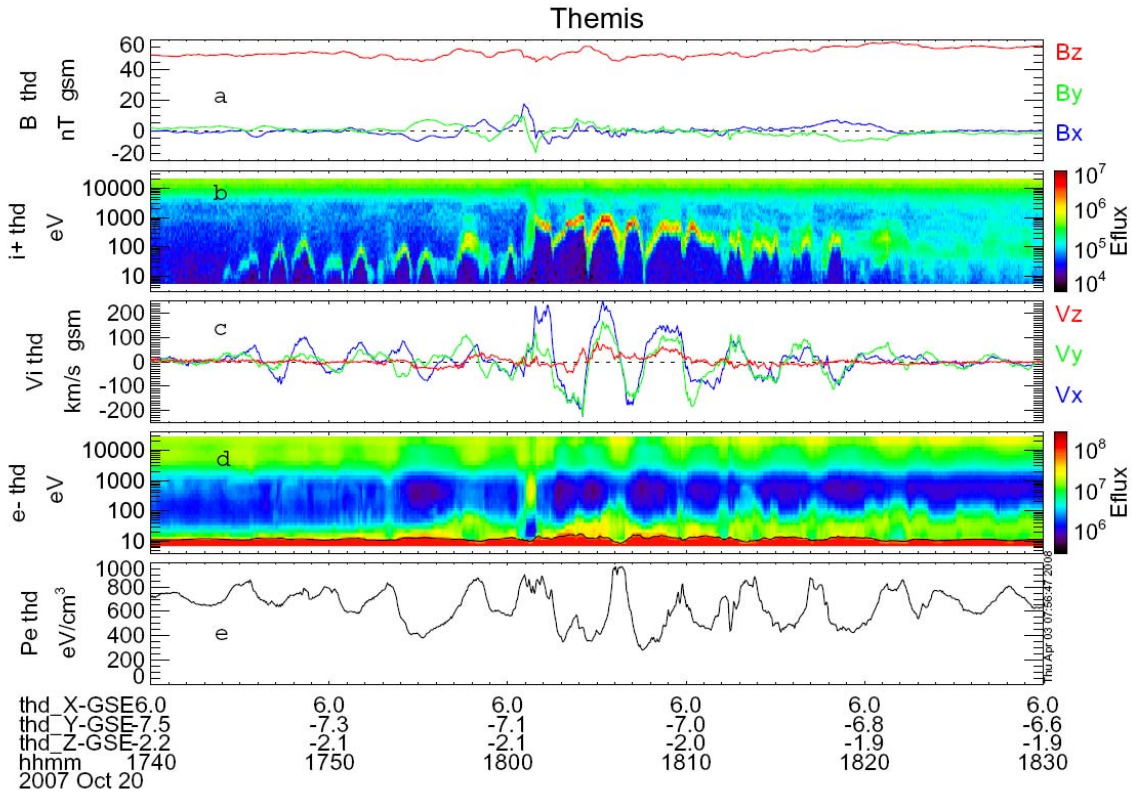

Figure 5: Ion spectrogram (panel 1), ion velocity (panel 2), electron spectrogram (panel 3), and electron total pressure measured by the ESA (panel 4) during a toroidal Pc 5 field line resonance (FLR). Cold ion stand out in the spectrogram, accelerated to keV energies by this wave. Ion velocity is slightly underestimated as explained in the text. Significant modulation of the electron pressure is observed in both the ESA (panel 4) and at higher energies by the SSTs.

Figure 5 shows an unusually large toroidal Pc 5 event. Since the spacecraft is near the node at the equator, the magnetic field variations are small (panel a). The resonance motion is easily seen in the ion spectrogram (panel b) where cold plasma (n_c~1 cm^{-3}) is accelerated to nearly keV energies by the wave. These resonances have been extremely helpful in identifying the cold plasma component near dawn, which often has a density between 0.1 cm^{-3} and 1.0 cm^{-3}. Panel c shows the ion velocity determined from the onboard moments (assuming only protons). The dominant amplitude during the wave growth period (prior to 1805 UT) is in GSM x-direction. The subsequent wave decay has nearly equal x and y components, as expected for a toroidal wave at a position of ($6R_e$, $-7R_e$, $2R_e$). Panel c shows that the hot electron component is strongly modulated by these waves, with nearly order of magnitude pressure variations being observed in the largest events. This pressure modulation may indicate a role that toroidal Pc 5 waves play in electron energization, or may just be the result of a pre-existing azimuthal pressure gradient. A modulation of the ion pressure can also be observed when ESA and SST data are combined.

For future studies of FLRs, there are some measurement problems that can limit the accuracy of the calculated plasma moments. First, the ion density may be overestimated and the ion velocity may be underestimated, due to a calculation error

caused by the energetic electron flux (panel c). Energetic electrons scattering into the ion sensor produce a small number of counts at low energy that mimic a tenuous, isotropic ion component. For example, at the peak in the flow velocity around 1806 UT, the background from scattered electrons adds ~25 counts/spin/energy. This background causes a ~0.4 cm^{-3} error in the calculated density, primarily from the lowest few energy bins. Since cold plasma (~1.4 cm^{-3}) and hot plasma (~0.14 cm^{-3}) have about four times this density, the velocity moment, given by flux/density, is underestimated by ~25% if this background is not removed. A second source of error is a consequence of the high energy cutoff of the ESA. When the ions are very hot, a substantial fraction of the ion flux may not be measured by the ESA resulting in an underestimation of density, velocity and pressure. For these events, the inclusion of SST measurements into the plasma distribution is generally required for accurate moment computations.

2.4 Low Latitude Boundary Layer during Northward IMF

The low latitude boundary layer (LLBL) is a dynamic region whose structure changes dramatically with local time and with orientation of the IMF. During northward IMF, the LLBL forms a thick layer with trapped magnetosheath plasma and small flows. During southward IMF, the LLBL is much thinner and contains reconnection flow jets and flux transfer events as described in section 2.5. Gosling et al. (1990) was the first to recognize the existence of a layered magnetopause, and Fuselier et al. (1995) and Le et al. (1996) have used observations of this layering to deduce its large scale structure and the dynamics of its formation. In this section we provide an example of THEMIS observations in the sub-solar region during northward IMF when a plasma depletion layer forms and dual-lobe reconnection traps magnetosheath plasma onto closed field lines. The ability of THEMIS to provide simultaneous, closely spaced observations at the magnetopause offers a unique opportunity to resolve the LLBL layers. In particular, the ESA instrument is ideally suited to provide information on topology and history of the various layers while the multipoint measurement differentiates the spatial from temporal evolution of features within the LLBL.

Figure 6 illustrates the spatial and temporal structure of the sub-solar LLBL revealed by THEMIS during northward IMF. The figure shows the magnetic field, density, velocity, and ion and electron spectrograms as THC and THD traveled from the magnetosheath to magnetosphere. The spacecraft were closely spaced, separated by about [-400, 700, 160] km in GSE coordinates. During this crossing the upstream magnetosheath plasma was highly striated, with large density and magnetic field variations associated with mirror mode waves (panels a, e). The initial crossings of the magnetopause at 0820 and 0826 UT showed a relatively thin boundary layer with no indications of a plasma depletion layer (PDL). THD observed a large ion hole (Turner et al., 1977) on the inbound crossing at 0820 UT, but not on the outbound crossing minutes later. THC may also have observed the edge of this ion hole on its inbound crossing, but measured a much smaller decrease in magnetic field strength.

After returning to the magnetosheath both spacecraft again approached the magnetopause, this time observing a PDL from ~0850 until ~0910 UT. 0910 UT marks

the outer edge of the boundary layer as indicated by heated electrons (panels e and j). Multiple ion holes were observed by each spacecraft within the PDL, and the close proximity of these holes to the mirror mode waves suggests the holes evolved from the waves. The field decreases in the magnetic holes were correlated between the two spacecraft, with simultaneous large decreases for 3 events and combinations of large/small decreases for 6 other events, all between 0852 and 0908 UT. These correlations indicate the scale size of the ion holes is about the spacecraft separation perpendicular to the magnetic field, ~800 km. This is about the same scale size estimated from an average perpendicular flow velocity (~30 km/s) times the typical duration of the ion holes (~30 s). For the ion holes in Figure 3 whose core fields are between 5 and 10 nT, the scale size of these holes is a few thermal ion (~100 eV) gyro-radii.

THC enters the boundary layer at ~0908 UT, as indicated by the tenuous energetic tail in the electrons (panels e), followed by THD at ~0912 UT. THC briefly crosses into the magnetosphere (0913-0916 UT) before re-entering and remaining in the boundary layer for ~10 minutes, followed by an final crossing into the magnetosphere (~0927 UT). For all but the outermost contact of the boundary layer, THC measured bi-directional heated electrons. Similarly, THD measured primarily bi-directional heated electrons in the boundary layer. These observations are consistent with other THEMIS observations of the sub-solar LLBL (McFadden et al., 2008c) which showed primarily bi-directional heated electrons during northward IMF indicating dual-lobe reconnection. These and other THEMIS observations at the magnetopause, which combine multi-satellite measurements with 3 s resolution of the plasma, should allow THEMIS to completely characterize the LLBL during its mission.

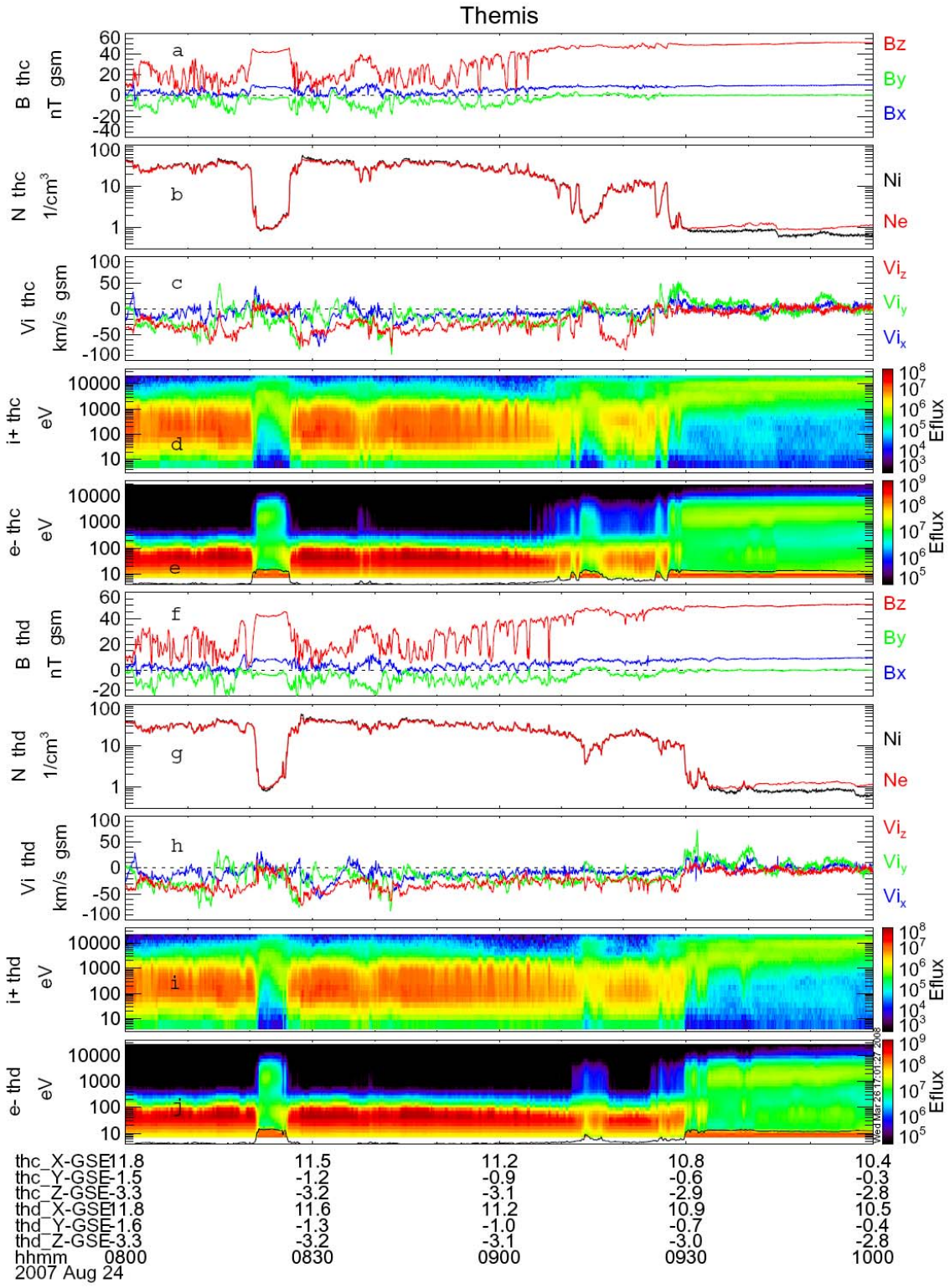

Figure 6: Magnetic field (panel a), ion (black) and electron (red) densities (panel b), ion velocity (panel c), and ion (panel d) and electron (panel e) spectrograms during a LLBL crossing near the subsolar point by THC. Panels f-j are the same for THD.

2.5 Magnetopause Reconnection and FTEs during Southward IMF

The early THEMIS mission, where all five probes crossed the equatorial magnetopause with spacecraft separations varying from a few hundred kilometers to ~10,000 km, provides an ideal data set for exploring ion-scale physics associated with dayside low-latitude reconnection. Spin period resolution of the plasma distribution functions, when combined with high resolution magnetic and electric field measurements, allows detailed studies of magnetopause structure. Early results published in a special issue of Geophysical Research Letters include: 1) multi-satellite observations of asymmetric reconnection demonstrating that the Hall electric fields are significant only on the magnetospheric side of the magnetopause (Mozer et al., 2008), 2) interactions of kinetic Alfven waves with particles at the magnetopause (Chaston et al, 2008), 3) multi-satellite observations of a crater flux transfer event (FTE) that is used to recreate the 2-D structure of the magnetopause (Sibeck et al., 2008), and 4) additional analyses of FTE structure (Lui et al., 2008; Liu et al., 2008).

FTEs are a common feature of the dayside magnetopause. They are believed to result from multiple reconnection lines forming plasmoids or flux ropes in a manner similar to plasmoid formation in the magnetotail. FTE signatures were initially observed in magnetometer data (Russell and Elphic, 1979), which displayed a variety of signatures (Elphic, 1995). The plasma signatures of FTEs were observed later (Paschmann et al., 1982) and MHD simulations are now manifesting similar structures (Raeder, 2006). Active FTEs, ones that are dynamically being generated, can be determined by the presence of large velocity variations within and near the FTE. Simultaneous measurements upstream and downstream should provide information on the boundary conditions necessary for their formation. In particular, THEMIS ESA measurements should provide the topology and history of the plasma populations which interacted during the formation of the FTE. Below we present THEMIS observations of a magnetopause crossing that demonstrates some of these capabilities.

Figure 7 shows a THEMIS magnetopause crossing during southward IMF. The current sheet crossing between 0834 and 0838 UT (panel a) was accompanied by reconnection flow jets (panel b) as expected for southward IMF. Prior to this crossing, evidence of earlier reconnection can be seen from at least nine FTE signatures. FTEs can be identified from both the magnetic field (panel a) and the plasma velocity (panel b), which are displayed in LMN coordinates. In addition, cold plasma adjacent to the magnetopause becomes visible in the ion spectrogram (panel c) due to bulk motion resulting from the passage of the FTEs. Cold plasma is also revealed by the mismatch of ion and electron densities (panel e) except during periods of bulk motion.

As shown in McFadden et al. (2008b), cold ions can be captured in the FTEs indicating that cold ions at the magnetopause do not suppress reconnection. The FTE at 0750 UT provides a particularly clear example of this capture. The reconnection of closed flux tubes containing cold ions is demonstrated from the electron spectrogram (panel d), whose energetic magnetospheric population is lost. Within the FTE, sheath electrons (~100 eV) replace the hot magnetospheric and cold ionospheric populations. The ~100

eV electron component inside the FTE is anisotropic, with matching counterstreaming field aligned components, and with field aligned fluxes five times larger than the perpendicular flux. An interesting aspect of these FTEs is the factor of 2-3 higher density inside the FTE as compared to outside the FTEs (panel e). This increase appears to occur before sheath plasma arrives suggesting compression of the cold component. However, it is not simply compression of the flux tube since the magnetic field dominates the pressure and it remains relatively constant. Whether this is a snowplow effect of the FTE, or just a density gradient in the cold plasma between the location the FTE traps the cold plasma and is later observed, is not known and will require investigations of more events. It is anticipated that these and other high resolution observations during southward IMF will allow a comprehensive study of the structure of FTEs.

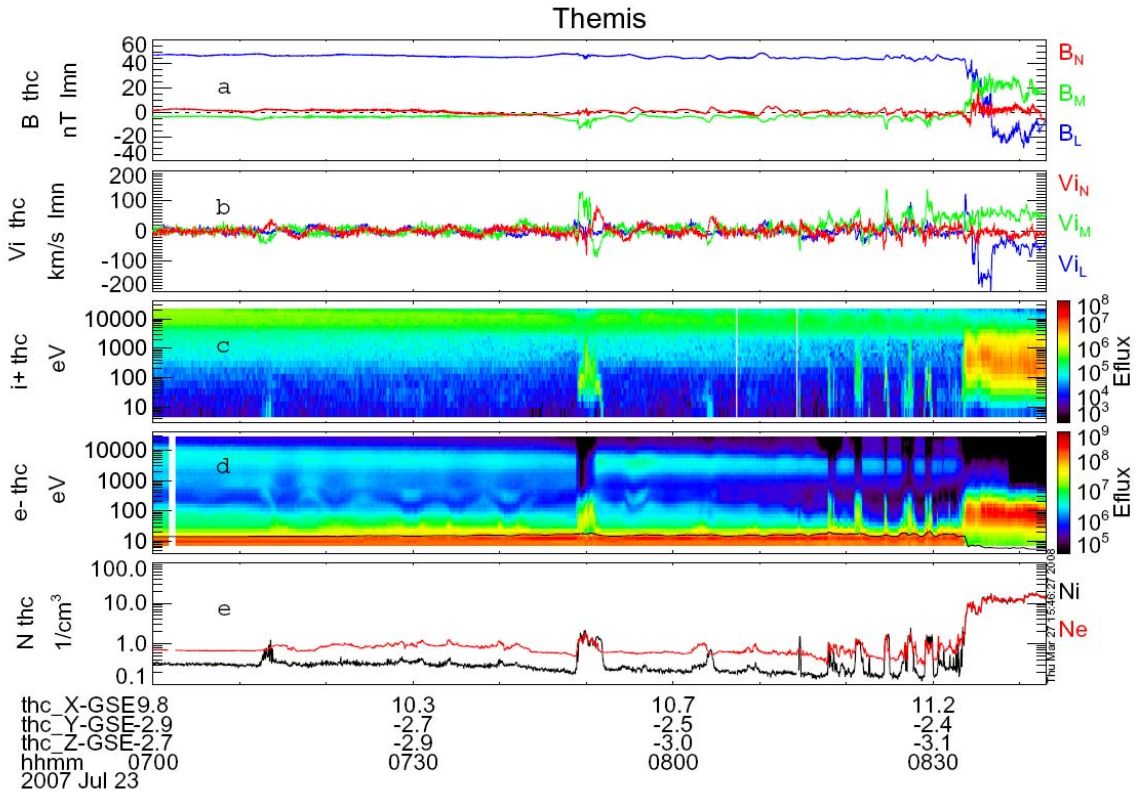

Figure 7: a) Magnetic field, b) ion velocity, c) ion spectrogram, d) electron spectrogram, and e) ion (black) and electron (red) densities. FTEs observed on the magnetospheric side of the magnetopause capture cold ions (panel c) and excite a weak FLR (panel b, 0715-0750 UT). The cold ions are only measured (panel e) when bulk motion allows them to penetrate the ~15V spacecraft potential.

An additional feature of this magnetopause crossing is the small but periodic modulation of the plasma velocity between 0710 and 0750. The magnetic field has a signature of an FTE at ~0712 UT, just at the start of the FLR ringing, suggesting the FTEs is the driver. Additional evidence for an FTE source for this FLR can be found in the 3 minute periodic FTEs found adjacent to the magnetopause, twice the 6 minute period of the FLR. Finally, we note that the FLR interacts with the electron distribution (panel d) producing enhancements and dropouts in the few hundred eV electrons. Further investigation of these plasma signatures, and the interactions between FLRs and FTEs,

should provide a much better understanding of the dynamics of a reconnecting magnetopause.

2.6 Bow Shock

The Earth's bow shock has been observed and cataloged by numerous satellites which have revealed a complex structure whose dynamics is primarily controlled by the orientation and magnitude of the interplanetary magnetic field (IMF) relative to the shock normal. Comparisons of these measurements with theory have provided a foundation for understanding numerous other collisionless shock phenomena including planetary shocks, interplanetary shocks, the heliosphere's termination shock, interstellar shocks, and intergalactic shocks. The variety of structure observed at the Earth's bow shock is impressive. It includes gyrating ions upstream of the quasi-perpendicular shock, the wave-like structure and reformation of the quasi-parallel shock, upstream foreshock particles that precondition the solar wind, Short Large Amplitude Magnetic Structures (SLAMS), Hot Flow Anomalies (HFAs), ion holes, 30 s period wave modulations of the upstream IMF, and a variety of higher frequency waves (whistler, Langmuir) and wave structures (electron solitary waves). During the first 9 months of operations, all of these phenomena have been observed except for high frequency wave phenomena which THEMIS does not measure. THEMIS multi-point observations of bow shock phenomena, with separations varying from ~200 km to ~10,000 km should provide new and important information about shock formation and stability, and about the 3-D structure and propagation of various upstream phenomena. Cross-correlation of the particle and fields signatures on multiple satellites should resolve the propagation direction, wave growth rate, particle thermalization rate, and effect of energy transfer on the shock.

Figure 8 shows an example of THC observations at and upstream of the quasi-parallel bow shock. After crossing the shock at ~0053 UT, the spacecraft spent significant time in the upstream region sampling a plasma dominated by 30 s waves (panel a). Foreshock ions propagating upstream of the shock are seen at energies >2 keV (panel c). The shock moves outward and briefly touches the spacecraft at 0112 UT before retreating Earthward. The solar wind density is a nominal 6/cm^3 and the velocity nearly 500 km/s. These observations reveal the complicated structure upstream of a quasi-parallel shock.

The upstream observations contain significant density turbulence (panel e). This turbulence was virtually identical on the three inner probes whose separations were less than 300 km. Within this turbulence one can identify several density holes (Parks et al., 2006), the most prominent appearing at 0121:30 UT. This hole had a factor of ~4 drop in density and is associated with a small shear in the magnetic field (panel a). Density holes may be related to hot flow anomalies (HFAs), another upstream structure that has been observed by THEMIS (Eastwood et al., 2008). HFAs are thought to result from a tangential discontinuity intersecting the bow shock (Schwartz, 1995), which causes upstream reflection of ions and an associated pressure that creates a low density, low

magnetic field channel. Multi-satellite observation by THEMIS, with 3 s resolution of the plasma, may be able to determine any connections between these disparate phenomena.

We end this discussion of shock observations with a caution about THEMIS observations in the solar wind. During the first 9 months, THEMIS plasma sensors were operated almost exclusively in magnetospheric mode, which has 32 sweeps per spin (11.25^o resolution). To fully resolve the solar wind beam, which is generally ~6^o wide, the ESA sensor should be operated in solar wind mode which has 64 sweeps/spin (5.6^o resolution). The observations in Figure 8, which show excellent agreement between ion and electron densities, suggest that the nominal magnetospheric mode was adequate for this event. The upstream turbulence during this event has likely broadened the solar wind beam, allowing 11.25^o resolution to be adequate. Finally, the solar wind density was nominal at this time so that counter saturation was not a problem. This is not always the case during solar wind encounters. For those using THEMIS data, a good indication of instrumental problems resolving the solar wind is a poor agreement between electron and ion density. An example can be found in the companion paper. See Figure 14 in McFadden et al. (2008a), where ion density is underestimated, as compared to the electron density, when measurements are made in the solar wind.

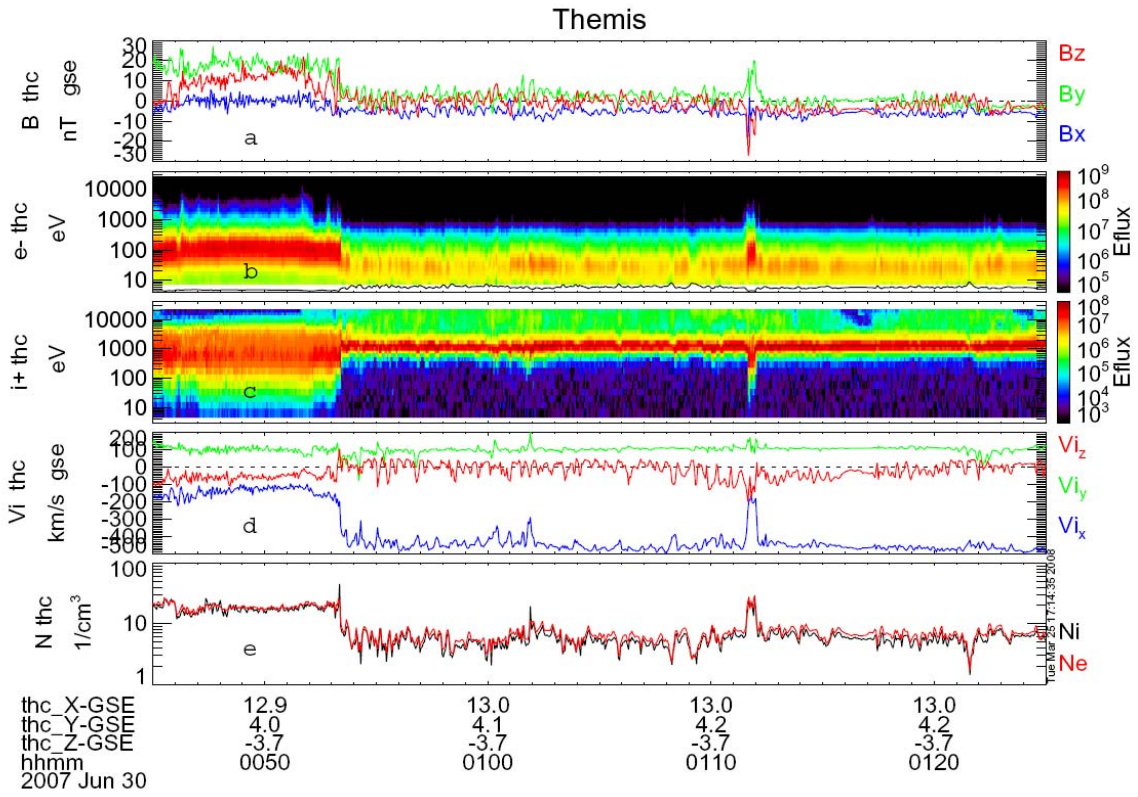

Figure 8: Magnetic field (panel a), electron (panel b) and ion (panel c) spectrograms, ion velocity (panel d), and ion (black) and electron (red) densities (panel e) near a quasi-parallel bow shock. 30 s waves (panels a and d) dominate the turbulent upstream region, along with energetic gyrating ions (panel c).

3.0 Performance Issues

Before embarking on analysis of the THEMIS ESA data, it is important for the scientist to be aware of various performance issues with the ESA: sources of background, non-ideal response of the instrument, limitations due to missing information, and telemetry formatting problems. The data set is too large for a subset of problem data to be routinely corrected or purged from the files. Instead the scientist should be aware of these data limitations in order to avoid periods where non-geophysical interference or missing information can result in misinterpretation of the observations. In this section we outline known performance issues associated with the THEMIS ESA data that were uncovered during the first nine months of operations.

3.1 Sources of sensor background counts

When performing detailed analysis of data from the THEMIS ESAs, care should be taken to assure that non-geophysical sources of counts do not affect the result. There are several sources for this background: 1) Solar UV scattered directly into the detector, 2) photoelectrons produced by solar UV that reach the detector, 3) energetic electrons scattered through the sensor to the detector, and 4) penetrating radiation.

3.1.1 Scattered UV

Scattered solar UV to the detectors was estimated from a ~140 min period on January 29, 2008 when THB was in the lobes and fast survey data were collected. Ion counts were negligible during this period, and MCP detector background rates were ~0.8 Hz per 22.5 degree anode. Sunlight background rates were determined from sun-viewing solid angle sectors, with the spin dependence of sunlight mapped from the energy sweep. Peak rates were <20/s summed over all anodes, and sunlight contamination was confined to ~10 degrees of rotation. This compares well with previous instruments, such as Cluster-HIA which had peak sunlight count rates of ~50/s, or the FAST satellite where peak rates were ~650/s. For additional information on UV scattering in ESA detectors see Carlson and McFadden (1998).

3.1.2 Photoelectrons

Spacecraft photoelectrons are a source of non-geophysical counts in the electron ESA. This photoelectron contamination comes from three different sources: Langmuir sensors, spacecraft surfaces, and internal sensor surfaces. This contamination can often be removed from the measurement when the spacecraft potential is known. Photoelectrons with energy greater than the spacecraft potential generally escape into the plasma, therefore the spacecraft potential provides a relatively clean separation, or cutoff energy, between reflecting photoelectrons and the in situ plasma. However, there are photoelectrons that appear at energies above the spacecraft potential that may require consideration if precise measurements are required.

The most prominent photoelectron contamination comes from the Langmuir sensors as illustrated in Figure 9a. Spectral peaks at ~15 eV and ~28 eV are both due to this contamination which results from proper Electric Field Instrument (EFI) operation. The EFI electronics supplies a bias current to the sensors roughly equal to ~30% of the sensor's photo-emission current (Bonnell et al., 2008). This bias current allows the sensors to lose a significant fraction of their photoelectrons and to float slightly below the local plasma potential, Φ_{sc}. Therefore Langmuir sensor photoelectrons are accelerated to nearly $e(\Phi_{sc} - \Phi_{plasma})$ when they reach the ESA. At large spacecraft potentials, sensor photoelectrons dominate over spacecraft photoelectrons at energies of $\sim e\Phi_{sc}$, but can generally be eliminated from moment calculations since they are confined to only one or two energy bins. However, when a cold population of electrons is present in the plasma, as often happens in the inner magnetosphere, it may be difficult to cleanly separate the photoelectrons from the plasma. Current observations suggest most cold plasma electrons are warmer than the photoelectron population, so modeling this population may provide a reasonable separation in a moment computation.

In addition to the Langmuir sensor photoelectrons, the EFI has several other antenna surfaces (usher, guard and braid) that can be voltage biased relative to the sensors. On THC from May 26 to June 22, 2007, the usher and guard were biased 8 V negative relative to the Langmuir sensors producing photoelectrons ~8 eV above the sensor potential. These are illustrated in Figure 9b where the axial antenna introduces photoelectrons at ~10 eV into the polar angle bins of the ESA. Similar electrons from the radial sensors are not apparent. Prior to May 26 the usher was 6 V positive, but the guard was 20 V negative relative to the sensor, resulting in ~19 eV electrons above spacecraft potential. Although most of these electrons escaped to space, some are observed in the electron sensor, especially in the polar bins that look along the spacecraft surface and record photoelectrons from the axial sensors. After June 22, 2007, photoelectrons from the usher, guard, and braid generally appear at energies below the spacecraft potential. Similar photoelectrons were observed on THD and THE after their boom deployments (June 2-6, 2007) until the bias changes on June 22, 2007.

Starting July 20, 2007 the braid was driven at the same voltage as Langmuir sensor 1 (on THC, THD, THE) to improve the EFI response. Starting about October 29, 2007 on THD and THE, and November 6 on THC, the spacecraft entered portions of the orbit where the spacecraft body shadowed the Langmuir sensors each spin for ~25 ms. This resulted in the voltage on the shadowed sensor charging to -85 V relative to the spacecraft, the upper limit of the EFI power supplies. Since the braid on all four antenna were tied to sensor 1, the sunlit braids on antennae 2, 3 and 4 would produce a ~25 ms burst of photoelectrons that could be seen in the electron ESA as illustrated in Figure 9c between 15 eV and 60 eV. The antenna shadowing ended by November 9, 2007 on THD and THE. By November 16, the braid on THC was switched back to ground to prevent further contamination. The current plans are to change EFI operating modes during shadowing periods to prevent this contamination in the future.

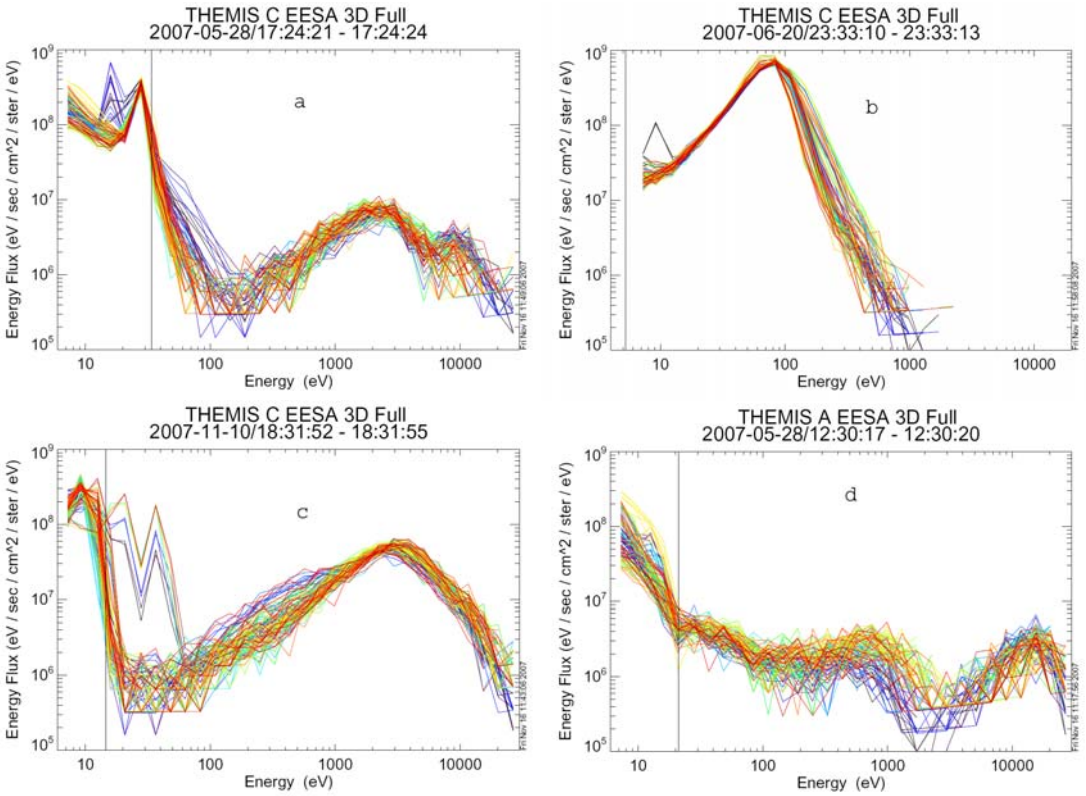

Figure 9: Electron spectra from 88 different solid angle look directions. The spacecraft potential relative to the plasma is indicated by vertical lines. a) photoelectrons from the axial (15 eV) and radial (28 eV) Langmuir sensors, b) a photoelectron peak (10 eV) above the spacecraft potential caused by the axial Langmuir sensor usher and guard being biased -8 V relative to the sensor, c) photoelectrons (15-60 eV) produced in a 25 ms burst when EFI sensor shadowing resulted in the EFI braids charging to -85 V relative to the spacecraft, and d) spacecraft photoelectrons at energies below the spacecraft potential measured prior to EFI boom deployment.

Spacecraft photoelectrons are the second most prominent contamination to the electron sensor. An electron spectrum taken prior to EFI boom deployment is shown in Figure 9d, with photoelectrons appearing below the spacecraft potential indicated by the vertical line at ~21 eV. Without EFI's measurement of Φ_{sc}, eliminating these photoelectrons from moment calculations is often difficult, with no clear spectral break to allow determination of Φ_{sc}. However, since photoelectrons are expected to have relatively constant spectra, Φ_{sc} could be estimated from the deviation between a measured low energy spectra and a characteristic photoelectron spectra.

Internally produced photoelectrons in the sensor aperture constitute a third form of photoelectron background. These electrons are produced over about 20^{o} of spacecraft rotation centered on the sunward direction and generally enhance only the lowest energy (<10 eV) bins. These electrons do not generally introduce errors to moment calculations unless the spacecraft potential is small, and small potentials occur during high densities which minimized their impact on moments. Since they are confined to low energies and a few angular bins that look toward the sun, they can be easily removed from a distribution if needed for precise moment calculations.

3.1.3 Scattered and Secondary Electrons

A third source of background counts in ESA sensors results from internal scattering of primary plasma electrons and the production of secondary electrons by these primaries. For shallow angle incidence, electrons have a ~50% chance of forward scattering with little energy loss. To reduce the fraction of these electrons that reach the detectors, the analyzer surfaces are scalloped and roughened with ebanol-C to reduce forward scattering. However, incident primaries that strike surfaces near the analyzer entrance produce secondary electrons and degraded (in energy) primary electrons that can pass through the electron analyzer, mixing with lower energy incident primary electrons.

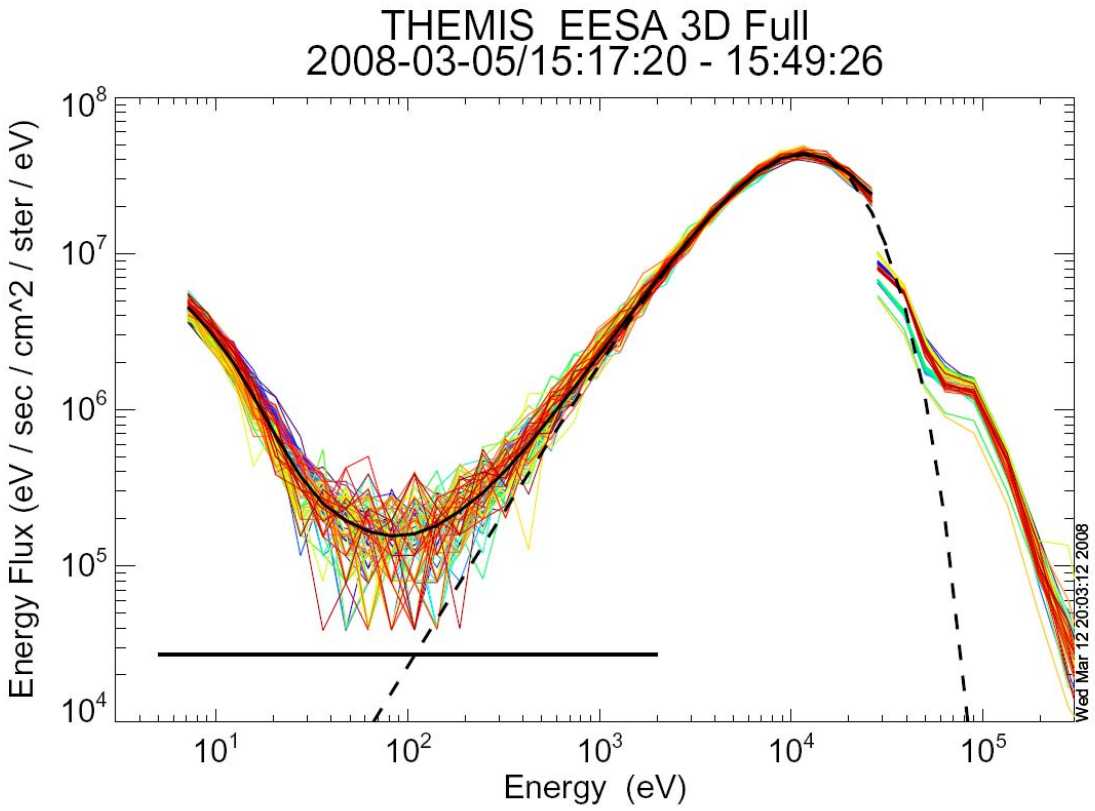

Figure 10: Electron spectra measured by the ESA (<30 keV) and SST (>30 keV) during an eclipse when the spacecraft charged to about -2000 V. The dashed curve is the expected spectrum for an energy retarded Maxwellian. Deviation from the Maxwellian at low energies (<1000 eV) is due to internally produced secondary and degraded primary electrons. The solid horizontal line represents an upper limit to directly scattered primaries reaching the detector, as determined from the ion sensor.

Figure 10 illustrates secondary electron production inside an electron ESA. The colored lines are electron spectra from the electron ESA (<30 keV) and electron SST (>30 keV). Different colors represent different look directions of the sensors, and the bunching of these spectra indicates the electrons were relatively isotropic. ESA data were formed by averaging six "snapshot" distributions, with each one spin snapshot taken every 128 spins. SST data were formed by averaging 12 snapshots over the same time interval. The black solid line that follows the electron spectra below 30 keV is the

average omni-directional spectra over the interval. The majority of electrons below 200 eV are internally produced secondaries and energy-degraded primaries as shown below.

The data in Figure 10 were taken while THB was in eclipse, so there are no photoelectrons contributing to the spectra. In addition the spacecraft had charged to about -2000 V, as determined from ion distribution functions, preventing low-energy in situ plasma electrons from reaching the sensor. Thus any primary electron registered at low energies, between the 0 to 1000 eV, must have initially been an electron between 2000 and 3000 eV in the plasma. Since the primary electrons are a good fit to a Maxwellian near the peak in the spectra, we use the dashed curve in the figure to show the expected differential energy flux of primaries after being retarded by the ~2000 V spacecraft potential. (Note: An energy shifted Maxwellian is still a Maxwellian). The deviation of the measured spectra from the dashed line at <1000 eV is due to secondary electrons and degraded primaries. Both of these populations are internally produced at the sensor aperture. Secondary electrons produced on spacecraft surfaces will not enter the ESA due to the large negative spacecraft potential.

The secondary and degraded primary spectra in Figure 10 are similar to atmospheric secondary and degraded primary spectra calculated by Evans (1974) to explain the shape of the auroral electron spectra. The main difference is that atmospheric secondary electron fluxes are about an order of magnitude larger since they build up over multiple electron bounces between the auroral acceleration region and the atmosphere. Therefore internally produced secondary electrons add only a small error to auroral plasma measurements. However, for THEMIS high altitude measurements, where the fluxes of low-energy electrons can be very small, errors due to secondary electrons can be significant. For the distribution shown in Figure 10, the error in the calculated density from including the internally produced secondaries is larger than the actual density.

In addition to secondary electrons, primary electrons can scatter directly to the detector producing additional background. The black line at the bottom of Figure 10 indicates an upper-estimate to the forward-scattered primaries as determined from background counts in the ion ESA. The ion sensor should record no ions at energies < 2000 eV during the interval used in Figure 10 since the spacecraft was charged to -2 kV. All ion sensor events recorded at <2 keV were therefore background from scattered ~10 keV electrons. (Ions have virtually no forward scattering.) Since the ion analyzer had a slightly larger gap between hemispheres than the electron analyzer, forward scattered primary electrons should be lower than the indicated level on the plot.

Scattered electrons can also create background counts in the ion ESA. The difference between electron and ion sensor sensitivity to this scattering results from the -2 kV potential at the front of the ion detector. This potential requires scattered electrons to be greater than 2 keV before they can be observed in the ion sensors, which virtually eliminates secondary electrons. However, observations show that even ~5 keV electrons produce insignificant background in THEMIS ion sensors. In general it is a >10 keV electron flux that introduces significant background counts.

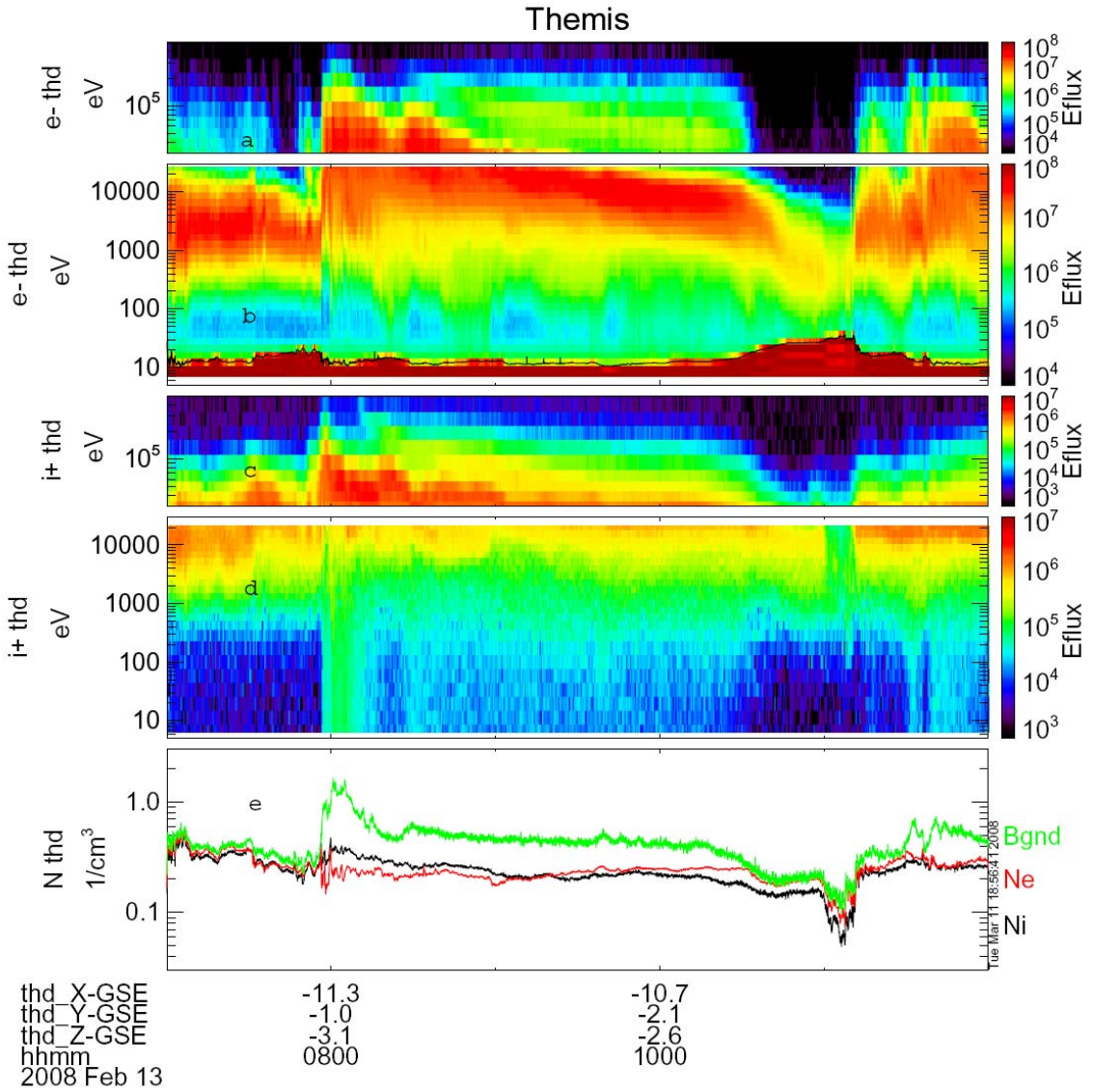

Figure 11: Panels a and b show electrons measured by the SST and ESA. Panels c and d are the same for ions. The figure illustrates problems caused by >10 keV electrons scattering into the sensors and producing counts at low energies (<500 eV, panel d; <40 eV, panel b). Panel e illustrates the over-estimated ion density (green) when these background counts are included in the density integral. The red curve is the estimated electron density integrated >40 eV, and the black curve is the estimated ion density integrated >500 eV. A more elaborate scheme to remove non-geophysical counts, and probably corrections for composition, are required to obtain better agreement between densities at this time.

Figure 11 shows an example of electrons scattering into an ion sensor. These observations are from THD within the plasma sheet. The upper two panels show energetic electrons measured by the SST (panel a) and the ESA (panel b). Panel c and d are the ion SST and ESA data, respectively. During periods when the >10 keV electron flux is high, as at ~8:00 UT, large increases in low-energy (<1 keV) ion counts are observed in the spectrogram (panel d). Most of the ion sensor's counts registered below 500 eV between 8:00 and 10:30 UT, and after 11:30 UT, are due to scattered energetic electrons. Panel e compares the uncorrected estimate of ion density (green), with the

electron density (red) illustrating the large errors in estimated ion density when energetic electrons are present. The black curve in panel e is the estimated in ion density determined from just the >500 eV ions, which agrees much better with the electron density. A more complicated calculation of ion and electron densities, with better rejection of background counts is required to get agreement at the 5% level. Finally, it should be noted that scattered electrons will also introduce errors in the ion flow velocity and temperature, in addition to these density errors.

3.1.4 Penetrating Radiation

A fourth source of background results from penetrating radiation as found in the inner magnetosphere. Generally these background counts become important at ~6 Re geocentric. This background produces flat spectra, with increasing count rate that peaks at ~4 Re. There is often a dropout of these background counts at perigee, as the spacecraft dips below the radiation belts. Background subtractions that reduce this contamination have been developed for the FAST mission (K. Seki, private communication), and could be applied to THEMIS if required for science analysis.

3.2 Errors due to Measurement Limitations

In this section, we remind the reader of the primary measurement limitations that can prevent precise calculation of plasma distributions and moments of the distributions. We begin with the limitations to the ESA plasma measurement, describing the primary missing components and their impact on moment calculations. Measurement limitations are also associated with invalid information from other instruments, and we elaborate on problems with EFI potential measurements and spacecraft attitude.

3.2.1 Lack of Composition Information

Although the THEMIS ESA plasma instruments provide an accurate measurement of the bulk of the plasma in most regions of the magnetosphere, this instrument does not measure all of the plasma, nor does it measure all the properties of the plasma. Significant errors can occur due to composition changes. THEMIS software developed for ESA data analysis assumes the measured ions are protons. In a density calculation, a higher-mass ion's contribution to number density will be incorrectly underestimated by the factor $(m/q)^{1/2}$. For example, consider a magnetosheath measurement where an alpha to proton ratio, N_α/N_p, is 10%. N_e will equal $N_p + 2N_\alpha$. However, the calculated ion density assuming protons, N_{ci}, will be given by $N_p + N_\alpha/\sqrt{2}$. This will result in $N_e/N_{ci} \sim 1.12$, or a ~12% difference in the calculated ion and electron densities. Mass density estimates can be skewed even more than number density, especially if significant oxygen is present.

Composition can also affect the velocity moment, with higher mass ions recorded as having higher velocity by the ratio of $(m/q)^{1/2}$. Therefore the fractional over-estimate of velocity will be similar to the fractional under-estimate in density for a plasma with non-proton components. Pressure is generally less affected by composition since pressure is

proportional to particle energy and the sensor measures E/q. However temperature, given by the ratio of pressure to density, can be affected by the error in the density.

3.2.2 Spacecraft Charging

Spacecraft charging may prevent the measurement of portions of the plasma distribution. Since spacecraft generally charge positive to attract photoelectrons (when in sunlight and when the density is less than ~300/cm^3), cold ions are often missed. As discussed in section 2.1, the cold ions often dominate the density within the dayside magnetosphere. These missed ions will also affect other moment computations such as temperature or flux. However, computations of the pressure and velocity are generally not affected by this missing plasma since cold ions contribute little to the pressure and since the velocity can often be well determined by the asymmetry of hotter plasma components.

Although spacecraft charging does not prevent the measurement of various electron components in the plasma, it can still result in distortions of the electron distribution that are difficult to correct. In particular, when a cold (~1 eV) ionospheric electron component is present in the plasma, as often occurs on closed flux tubes, these electrons are difficult to resolve. For example, spacecraft charging of 20 V will cause the ESA sensor to measure cold electrons at ~20 eV, where the ESA's intrinsic energy resolution and energy sweep result in energy bins whose width is ~6 eV. The temperature of these cold electrons will not be resolved. In addition, if spacecraft photoelectrons are present, these wide energy bins will detect a mixture of cold plasma electrons and photoelectrons that is difficult, if not impossible, to separate. Since a cold electron component often accompanies a cold ion component, accurate density measurements in plasmaspheric plumes is doubly difficult.

3.2.3 Finite Energy Range

The upper limit to the ESA's energy range can be another source of error when calculating moments. Within the plasmasheet or inner magnetosphere, the ESA's upper energy limit of ~25 keV for ions, and ~30 keV for electrons, often results in a significant fraction of the plasma being missed. The limited energy range primarily impacts the higher order moments, such as pressure, but can also affect density and velocity calculations. Figure 12 shows an example of plasma sheet measurements when both the ions and electrons extend above the ESA energy range (panels b-e). Panel f illustrates the fractional densities measured by the ESA and SST, while panel g illustrates the fractional pressures measured by these instruments. Clearly the ions measured by the SST are important for both the density and the pressure as illustrated in panels f and g. To obtain better density estimates, ion integrals only counted >1000 eV ions (to eliminate scattered electrons) and electron integrals only counted >40 eV electrons (to eliminate internally produced secondary electrons). We generally recommend that the SST data be combined with the ESA data when moment calculations are made in the plasma sheet or inner magnetosphere.

3.2.4 Limited Field of View

Two other measurement limitations in the ESA sensor are related to its field-of-view. Since the sensor only looks in a half-plane at any instant, time aliasing during a spin can skew the measurement. This is especially true for electron velocity moment calculations as illustrated in Figure 13, panels f-g. A few percent density variations during a spin can result in large (~100 km/s) errors in the calculated flows, depending upon the electron temperature. For THEMIS these errors are primarily confined to the spin plane since the sensor continuously measures in both directions along the spin axis.

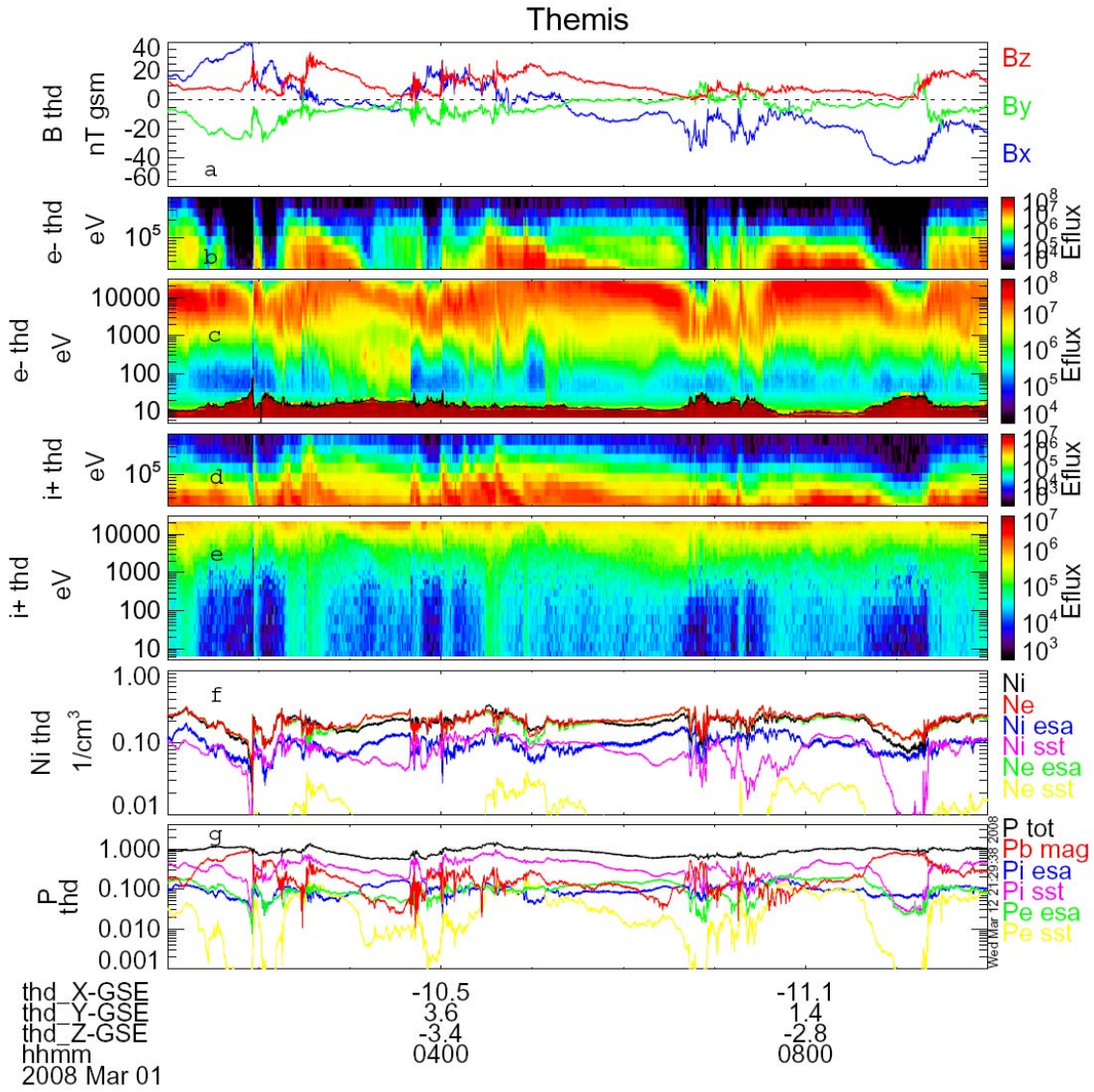

Figure 12: a) Magnetic field, b) SST electrons, c) ESA electrons, d) SST ions, e) ESA ions, f) density, and g) pressure. Density and pressure are broken down by components to show the fractional contributions from each instrument.

The second measurement limitation is the ~6° FWHM sensor field-of-view in the half-plane. Since nominal energy sweeps occur during ~11.25° of rotation, narrow beams might be missed. Examples of such narrow beams would include anti-earthward accelerated auroral electron beams and the solar wind ion beam. The ESA instrument has a solar wind mode with 64 sweeps/spin (5.6° resolution), that can resolve the solar wind ions, however it is not always used in the solar wind. In addition, the high ion count rates in the solar wind can result in significant dead time corrections to these data introducing additional errors.

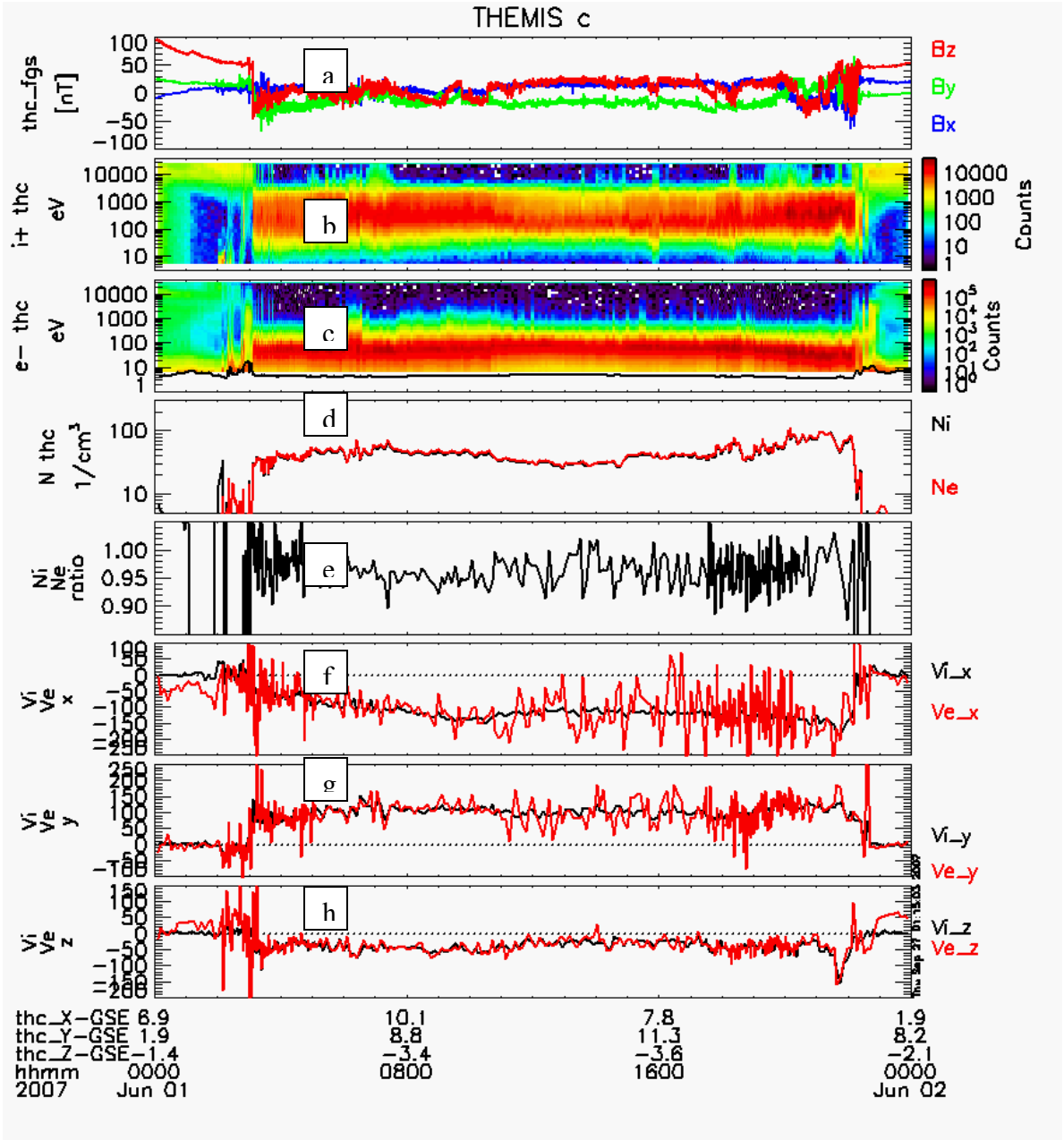

Figure 13: a) Magnetic field, b) ion spectrogram, c) electron spectrogram, d) ion (black) and electron (red) density, e) electron to ion density ratio, f-g) components of velocity. Panels f, g, and h illustrates the errors in the calculated electron velocity caused by small density fluctuations during a spacecraft spin. The density fluctuations are due to mirror modes in the magnetosheath.

3.2.5 EFI availability

Since knowledge of spacecraft potential is essential for correct transformations of measured counts to plasma distribution function, EFI measurements are required. Start dates where valid EFI potential measurements are initially available are listed in Bonnell et al. (2008). Prior to EFI deployments, spacecraft potential will have to be estimated from the plasma measurements alone. Even after EFI sensor deployment, there are periods where the EFI data may be less than ideal. The EFI Langmuir sensors are designed for sunlit conditions, therefore when the spacecraft are in eclipse the sensor potential does not provide a good estimate of spacecraft-to-plasma potential. During sensor diagnostic sweeps, which are occasionally run and can take several hours, spacecraft potential measurements can be invalid. The bias currents to the Langmuir sensors, and the associated voltages on adjacent surfaces, have been changed several times during the first year resulting in different functional relationships between spacecraft-to-sensor potential and spacecraft-to-plasma potential. Lastly, during periods with restricted telemetry rates, EFI data may not be at the same cadence as the plasma data, resulting in time aliasing problems at steep density gradients. Since there are several sources of, or data products with, spacecraft-to-sensor potentials and since these sources have variable time resolution, care must be taken to select the appropriate data type as an input to the plasma data calculations.

3.2.6 Measurements in Eclipse

One additional source of error in the plasma measurements can occur during eclipse, when sun-sensor data is unavailable to organize spin-synchronous plasma data. As sun pulses disappear, the spacecraft electronics will shift into a “fly-wheel mode” that assumes the spin rate is constant. However, small changes in spin period due to thermal contraction of the booms and fuel result in a drift in the orientation at the start of a spin. Although this drift is small, the accumulated error can be significant by the time the spacecraft exits the Earth’s shadow. The primary error is therefore in the orientation of vector and tensor quantities such as the plasma velocity and pressure tensor. Errors to scalar quantities such as density and temperature are negligible. In principle these orientation errors could be corrected with modeling, but at the time of this publication there are no plans to develop this code since shadow time data collection is not considered part of the baseline mission.

3.3 Errors due to Data Formatting Problems

At the start of the THEMIS mission, several data formatting problems in the ETC board were discovered. The ETC board processes the counts data from the ESA and SST, averaging and compressing these data before handing the data products to the instrument processor board for data packet formation. The ETC contains mapping tables that are loaded from a PROM at the start of a mode. For ESA 3-D data products (survey, burst and reduced data products), energy maps and an angle maps are used to direct and sum

the counter readouts into data product arrays. Early in the mission it was discovered that an occasional bit error could occur in the table load if the processor was simultaneously performing other tasks at the time. These bit errors generally caused some elements of the data product arrays to be zero and resulted in other data products receiving these counts. These bit errors were generally confined to only a few of the 30 3-D data products generated by the 5 satellites, with the subset of tainted products changing with each mode change. The misdirection of data was discovered early in commissioning phase, and software changes to eliminate processor conflicts during table loads were implemented on all spacecraft by April 27, 2007. Prior to this date, care should be taken in interpreting ESA data, especially any moment computations.

A second data formatting error occurs at the transition between instrument modes. Instrument mode transitions are associated with both configuration changes, such as transitions from magnetospheric mode to solar wind mode, and operational changes, such as transitions from Fast Survey to Slow Survey. In both cases, the transition between table maps and data packet formatting result in the loss of data. Depending upon the data product, and in particular the number of spin-snapshots in a data packet, these transitions can result in a data loss, or incorrectly formatted data, that lasts for a few seconds to a few minutes.

A third data formatting problem results from ETC counter saturation and is confined to reduced data products. During slow survey mode, reduced data packets are formed by averaging all counts over a spin into a single energy spectrum. High count rate data, such as electron data in the magnetosheath, often result in counter saturation at the peak in the spectrum. The ETC is designed not to overflow and saturation is easily recognized in the data as a flattened peak in the spectra. If the spectra are plotted as counts, the maximum count in any energy-angle bin is 65,535. During the most intense magnetosheath events, saturations may also be observed in the ion, slow-survey, reduced data products, or in the electron, fast-survey and slow-survey, reduced data products.

Early in the mission, data formatting problems also plagued the onboard moment computations performed by the ETC. In particular the same table load bit errors seen in the 3-D products were present in the moment calculations. Since the moment tables are several orders of magnitude larger than the 3-D data product tables, detection and correction of errors is nearly impossible. In addition, an error in the PROM resulted in the loss of one of the components of the velocity moment (Vy), and incorrect ordering of higher moment components in the moment data packet. Although some onboard moment data can be extracted from these early data, we strongly recommend working with THEMIS team members before incorporating any early-mission moment data in to science papers. Corrections to the flight software were not implemented until August 6, 2007, and additional problems with spacecraft potential corrections to on-board moments were present between November 18 and 22, 2007. Lastly, we point out that electron moments are generally invalid on until EFI boom deployments allow onboard corrections for spacecraft charging. For THB and THA these boom deployments were completed on November 18, 2007 and January 13, 2008, respectively.

4.0 Summary

The THEMIS ESA plasma instruments measure the 3-D distribution function of electrons and ions at 3 second cadence. Instrument design and calibration can be found in the companion paper (McFadden et al., 2008a), which includes a description of the in-flight calibration which provides very accurate inter-calibration of these sensors. In this first results paper we demonstrate the capabilities of the ESA instruments including their ability to resolve ion scale phenomena, to separate spatial and temporal structure, and to reveal new details of the dayside magnetosphere. Observations are presented of plasmaspheric plumes, ion conic outflows, field line resonances, the low latitude boundary layer, flux transfer events, and structure at the quasi-parallel bow shock. Although the highest-quality ESA burst data is limited to ~15 minutes per orbit, coarser 3-D plasma distributions at spin resolution are available for ~12 hours each orbit with adequate resolution for moment computation or detection of field-aligned beams. Even in the slowest data collection mode, spin-resolution energy spectra and onboard moment computations provide adequate information for interpretation of plasma structure. Accurate calibrations allow the combined electron and ion data to be used to deduce additional features about the plasma, including mass composition or the presence of missed cold plasma. These first result observations illustrate the capabilities of the plasma sensors and the synergy of its measurements with the other THEMIS experiments, demonstrating the successful achievement of all measurement objectives.

Last of all, we point out that THEMIS has an open data policy that strives for an immediate release of data to the community. These data are made available before data quality can be determined, or before the data can be validated. Therefore, this paper includes discussions of various performance issues with the ESA instrument, such as sources of sensor background, measurement limitations, and data formatting problems. It is hoped that this discussion provides scientists with an adequate reference so that understanding and correcting for these performance issues will allow full use of the THEMIS measurement capabilities while avoiding any misinterpretation of the observations.

Acknowledgements

The analysis of THEMIS data was supported by NASA NAS5-02099. Financial support for the work of the FGM Lead Investigator Team at the Technical University of Braunschweig by the German Ministerium für Wirtschaft und Technologie and the Deutsches Zentrum für Luft- und Raumfahrt under grant 50QP0402 is acknowledged.

References

V. Angelopoulos, et al., Space Sci. Rev., this issue, 2008.

U. Auster, K.-H. Glassmeier, et al., Space Sci. Rev., this issue, 2008.

J.W. Bonnell, F.S. Mozer, G.T. Delory, A.J. Hull, R.E. Ergun, C.M. Cully, Space Sci. Rev., this issue, 2008.

C.W. Carlson, and J.P. McFadden, Geophysical Monograph 102, p.125, 1998.

C.C. Chaston et al., Geophys. Res. Lett., in press, 2008.

R.C. Elphic, Geophysical Monograph 90, p. 225–233, 1995.

J. Eastwood et al., Geophys. Res. Lett., in press, 2008.

D. Evans, J. Geophys. Res., 79, 2853-2858, 1974.

S.A. Fuselier, B.J. Anderson, T.G. Onsager, J. Geophys. Res., 100, 11805, 1995.

K.-H. Glassmeier et al., Geophys. Res. Lett., in press, 2008.

J. Goldstein, B.R. Sandel, M.F. Thomsen, M. Spasojevic, P.H. Reiff, J. Geophys. Res., 109, A03202, doi:10.1029/2003JA010281, 2004.

J.T. Gosling, M.F. Thomsen, S.J. Bame, R.C. Elphic, and C.T. Russell, J. Geophys. Res., 95, 8073, 1990.

D. Larson, T. Moreau, R. Lee, R. Canario, and R.P. Lin, Space Sci. Rev., this issue, 2008.

W. Lennartsson and E.G. Shelley, J. Geophys. Res., 91, 3061-3076, 1986.

G. Le, C.T. Russell, J.T. Gosling, and M.F. Thomsen, J. Geophys. Res., 101, 27239, 1996.

A. Lui et al., Geophys. Res. Lett., in press, 2008.

J. Liu et al., Geophys. Res. Lett., submitted, 2008.

J.P. McFadden, C.W. Carlson, D. Larson, V. Angelopoulos, Space Sci. Rev., this issue, 2008a.

J.P. McFadden et al., Geophys. Res. Lett., in press, 2008b.

J.P. McFadden et al., Geophys. Res. Lett., in press, 2008c.

T.E. Moore, Revs. Geophys. (Suppl.), 1039-1048, 1991.

F.S. Mozer et al., Geophys. Res. Lett., in press, 2008.

M. Oieroset et al., Geophys. Res. Lett., in press, 2008.

G.K. Parks, E. Lee, F. Mozer, M. Wilber, E. Lucek, I. Dandouras, H. Rème, C. Mazelle, J.B. Cao, K. Meziane, M.L. Goldstein and P. Escoubet, Phys. of Plasmas, 13, 050701, 2006.

G. Paschmann, G. Haerendel, I. Papamastorakis, N. Sckopke, S. Bame, J. Gosling, C. Russell, J. Geophys. Res., 87, 2159, 1982.

J. Raeder, Annales Geophysicae, 24, 381–392, 2006.

A. Roux et al., Space Sci. Rev., this issue, 2008.

C.T. Russell, and R.C. Elphic, Geophys. Res. Lett., 6, 33-36, 1979.

S. Schwartz, Adv. Space Res., 15, 107-116, 1995.

J.A. Sauvaud et al., Annales Geophysicae, 19, 1523, 2001.

D. Sibeck, Geophys. Res. Lett., in press, 2008.

Y.J. Su, M.F. Thomsen, J.E. Borovsky, R.C. Elphic, D.J. Lawrence, D.J. McComas, J. Atmos. Solar-Terr Phy., 63, 1185, 2001.

J.M. Turner, L.F. Burlaga, N.F. Ness, and J.F. Lemaire, J. Geophys. Res., 82, 1921–1924, 1977.

A.W. Yau, P.H. Beckwith, W.K. Peterson, and E.G. Shelley, J. Geophys. Res., 90, 6395–6407, 1985.